Latest version M. Reiser

Abstract

Title of Thesis: Electron Gun Calibration and a New Design of the Energy Analyzer For Energy Spread Evolution Study

Yupeng Cui, Master, 2001

Thesis directed by: Professor Patrick O'Shea

Electrical and Computer Engineering Department

The University of Maryland Electron Ring requires a detailed knowledge of the energy spread of the beam. The evolution of energy spread in space-charge dominated beams is not well understood. A transport line with the length of 2.2m is being set up to study the energy spread evolution.

In this thesis, experimental studies are presented on the performance characteristics of the electron gun. Electron gun calibration has been completed and the initial beam envelope and emittance have been measured. An important achievement during this calibration work has been a big improvement in the electron beam temporal pulse shape.

The design for energy spread evolution experiment has been completed and all the focusing solenoids have been recalibrated. In the thesis, a theoretical calculation result of the energy spread evolution is presented.

Energy spread measurements of the electron beams in the range of several keV are very difficult and tricky. In this thesis, we report the design and simulation

of a new energy analyzer with a significantly improved resolution compared to the analyzer used earlier.

Acknowledgements

I would like to express my sincere gratitude to all the people contributing to my thesis work.

First of all, I would like to thank my advisor, Professor Patrick O'Shea for his professional advice and patient guidance during my thesis work. He has trusted my judgment, encouraged me, and supported me for my theoretical and experimental work. I would also like to thank Professor Martin Reiser. His support and encouragement have greatly motivated me to get the very important experiment results in the final stage of thesis. I would like to express my thanks to Dr. Rami Kishek, the manager for UMER, for useful advice and discussion about my thesis. I am also grateful to them for serving on the advisory committee.

I am thankful to Dr. Santiago Bernal for his great help and advice in my experiment. I would like to thank Dr. Agust Valfells cooperating with me for the new energy analyzer design. I would like to thank Dr. Terry Godlove at FMT and Mr. Bryan Quinn for their helpful advice and discussions during the electron gun calibration work. I am grateful to Dr. Yun Zou, the former graduate student whose work I continued, for transferring his knowledge of the facility to me. I am also grateful to Victor Yun and Mark T. Walter who provided invaluable help in the mechanical designs.

I am especially grateful to John Harris for his careful help and valuable advice to polish my English problem in the thesis. I would like to thank Hui Li,

Matt Virgo and John Neumann for their help. I am also thank Brian Beaudoin and Matt Glanzer providing me great help in my experiment.

At last, I am very grateful to US DOE providing fund for my experiment.

Table of Contents

List of Tables

List of Figures

Chapter 1

Introduction

In the University of Maryland Electron Ring (UMER) lab, theoretical and experimental work has been carried out for some time to study space charge dominated beams. Energy spread of the charged particle beam is an interesting topic and has many applications. For example, in ion microscopy, large energy spread will prevent the beam from being focused into a small spot. Cold electron beams are very useful to cool ion beams so that their energy spread and transverse temperature becomes very low.

We know when the particles are accelerated, the beam cooling will happen in the longitudinal direction [1]. Another effect of accelerating the beam is to increase the interparticle spacing in the axial direction. The energy transfer mechanism is via Coulomb collisions. This is known as the longitudinal-longitudinal effect [2]. After acceleration, the beam will not be in thermal equilibrium, with the transverse temperature higher than the longitudinal temperature. Coulomb collisions, instabilities, etc. will drive the beam towards equilibrium lowering the transverse temperature and increasing the longitudinal temperature, which results in the longitudinal energy spread evolution directly. This is known as the Boersch effect [3].

An experiment is being set up to measure the longitudinal energy spread evolution in UMER lab. The experimental transport line with a length of 2.2 m will consist of electron gun, four short solenoids, one long solenoid and two energy analyzers. Two energy analyzers are used at the two point of the transport line.

The calibration of the electron gun, which will be used in the energy spread evolution experiment, has been completed and the initial beam envelope and emittance have been measured. During this calibration work, the forming process of the pulser signal in the electron gun has been analyzed using the reflection wave theory. An important achievement has been a big improvement in the electron beam temporal pulse shape.

Design for energy spread evolution experiment has been finished. According theoretical calculation, the longitudinal energy spread evolution is very small in this experiment, about several eV in a limited long transport line. To measure such small energy spread in the experiment, the energy analyzers must have good resolution.

Other graduate students have conducted pioneering research work in energy spread measurement, using initially a parallel plate energy analyzer and later a cylindrical analyzer. The resolution of the cylindrical analyzer is greatly improved compared to the parallel plate analyzer, but it still cannot satisfy needs of UMER and energy spread evolution experiment. In this thesis, I describe improvements to the cylindrical analyzer. The simulation resolution is very good for the new

structure analyzer. For 10 keV beam, the resolution can get to 0.5 eV. This energy analyzer is being built now. I report about the design and simulation result of the new energy analyzer in this thesis.

The thesis mainly focuses on the electron gun calibration and new energy analyzer design, which are the preparations for the energy spread evolution study. Chapter 2 presents the longitudinal energy spread evolution theory. Chapter 3 shows experimental result of electron gun calibration and the improved pulser signal. Chapter 4 describes the focusing magnetic fields, beam match, and theoretical calculation result for energy spread evolution experiment. Chapter 5 describes the design and simulation of the new energy analyzer.

Chapter 2

Energy Spread Evolution Theory

2.1 Introduction of Longitudinal Energy Spread Evolution

Theoretical understanding of energy spread evolution in charged-particle beams, from emission to equilibrium, is still not well understood [1, 2]. There are three main physical processes involved: cooling due to acceleration, longitudinal-longitudinal effects, and the Boersch effect.

When the particles come off the emitter the beam is in thermal equilibrium (i.e. the transverse and longitudinal temperatures are equal). This implies that the energy spread in the transverse direction is the same as that in the longitudinal direction. When the particles are accelerated the energy spread remains constant, but the longitudinal velocity spread decreases and hence the longitudinal temperature decreases. Equation (2.1) describes the relation between the initial longitudinal temperature, $T_{\|i}$, and the longitudinal temperature immediately after acceleration, $T_{\|f}$ (see Equation 5.339 in Reference [1])

$$k_B T_{\|f} = \frac{(k_B T_{\|i})^2}{2qV_0} \qquad (2.1)$$

where k_B is the Boltzmann's constant, q is the electron charge and V_0 is the accelerating high voltage.

For instance a beam that comes off the emitter with a temperature of 0.1 eV and is accelerated by 5 kV voltage can be cooled to a temperature of 10^{-6} eV.

Another effect of accelerating the beam is to increase the interparticle spacing in the axial direction. Since the acceleration time is short compared to the charged particle plasma period, this increase occurs mostly after acceleration. The transfer mechanism is via Coulomb collisions. This is known as the longitudinal-longitudinal effect. Equation (2.2) gives the energy spread after acceleration [1, 2,4]

$$\Delta\widetilde{E}_{\|f} = \left[\frac{C}{\pi\varepsilon_0} q n^{1/3} q V_0 + 2 q V_0 k_B T_{\|f}\right]^{1/2} \qquad (2.2)$$

The first term on the right-hand side of (2.2) is due to the longitudinal-longitudinal effect, with C being a constant on the order of unity and n being the particle density.

After acceleration the beam will not be in thermal equilibrium, with the transverse temperature higher than the longitudinal temperature. Various effects such as Coulomb collisions, instabilities, etc., will drive the beam towards equilibrium, lowering the transverse temperature and increasing the longitudinal temperature. This is known as the Boersch effect [3]. The longitudinal heating of the beam will manifest itself as an increase in the longitudinal energy spread of the beam, since we have the following relation (see Equation 5.325a in Reference [1])

$$\Delta\widetilde{E} = \sqrt{2 q V_0 k_B T_{\|}} \qquad (2.3)$$

So the energy spread scales like the square root of the temperature. One of the mechanisms leading to equilibrium is Coulomb collisions. If one assumes that this is the only mechanism [5] at play one gets the following equation for the temporal development of the longitudinal temperature (see Equation 6.156b in Reference [1])

$$T_{\parallel} = \frac{2}{3} T_{\perp i} (1 - e^{-3t/\tau_{eff}}) \qquad (2.4)$$

The effective temperature relaxation time τ_{eff} is dependent on the particle density of the beam and the initial transverse temperature, $T_{\perp i}$. As an example, for a 5 keV beam, we note that for particles coming off the emitting surface with a temperature of 0.1 eV, cooling down through acceleration and subsequently heating up to a temperature of 0.067 eV via the Boersch effect, the longitudinal energy spread will go from 0.1 eV at the emitter to 26 eV at equilibrium.

2.2 Organization of Experiment

To measure the energy spread evolution, an experiment will be performed along a 2.25 m transport line measuring the longitudinal energy spread at two points. We will use a thermionic triode gun with a variable accelerating potential ranging from 3-5 kV and current ranging from 70-135 mA. The beamline will have three short solenoids for matching into a long solenoid and one short solenoid for matching into a diagnostic chamber. One energy analyzer is situated between the second and third short solenoids and may be retracted from the path of the beam.

This analyzer is placed at a beam waist. The second energy analyzer is located at the end of the beamline. The distance between the two analyzers is 184 cm. Figure 2.1 shows a schematic drawing of the experiment where M1, M2, M3, and M5 are short solenoids. The long solenoid, M4, serves as a uniform focusing channel. Two current monitors are included to monitor possible beam loss.

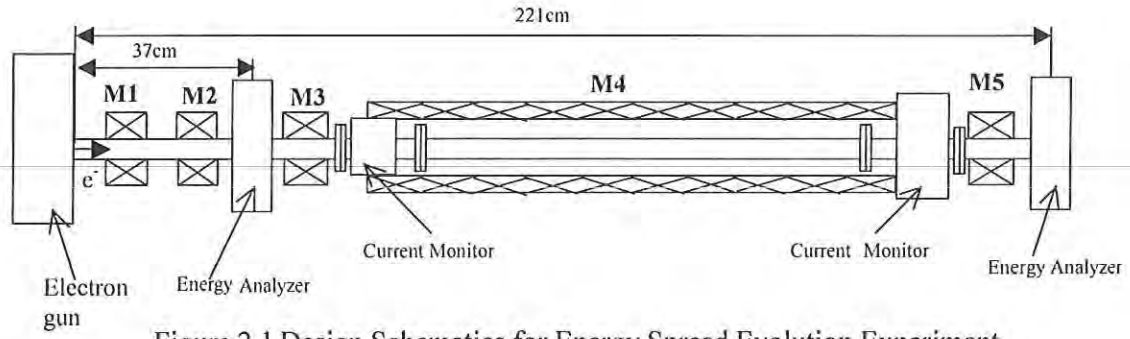

Figure 2.1 Design Schematics for Energy Spread Evolution Experiment

Chapter 3

Electron Gun Calibration

3.1 Purpose of Electron Gun Calibration

The electron gun used in the experiment is a variable-perveance gridded gun developed and constructed at the University of Maryland [6]. This gun has extremely flexible design features and can produce a wide range of beam parameters. The reasons we calibrate the electron gun are: first, the energy spread growth experiment needs known initial beam conditions to match the beam along the transport line; second, because the cathode of the gun was changed, the new performance characteristics of the gun are needed to re-calibrate to find electron gun structure and sum up the operating parameters as a document for future so as to have a comparison with UMER gun [7]; last, it is helpful to know how to get a better-shaped beam pulse by studying electron gun theory and performance.

3.2 Description of the Electron Gun

Figure 3.1 shows the detailed mechanical drawing of the electron gun [6]. The electron cathode assembly has a Pierce-type geometry and a planar configuration consisting of the heater, cathode and grid. The radius of new cathode is 4mm and heating area is around 0.5 cm^2 [8]. With such a small heating area, the heating inhomogeneity is not a problem. The grid consists of tungsten wire coated

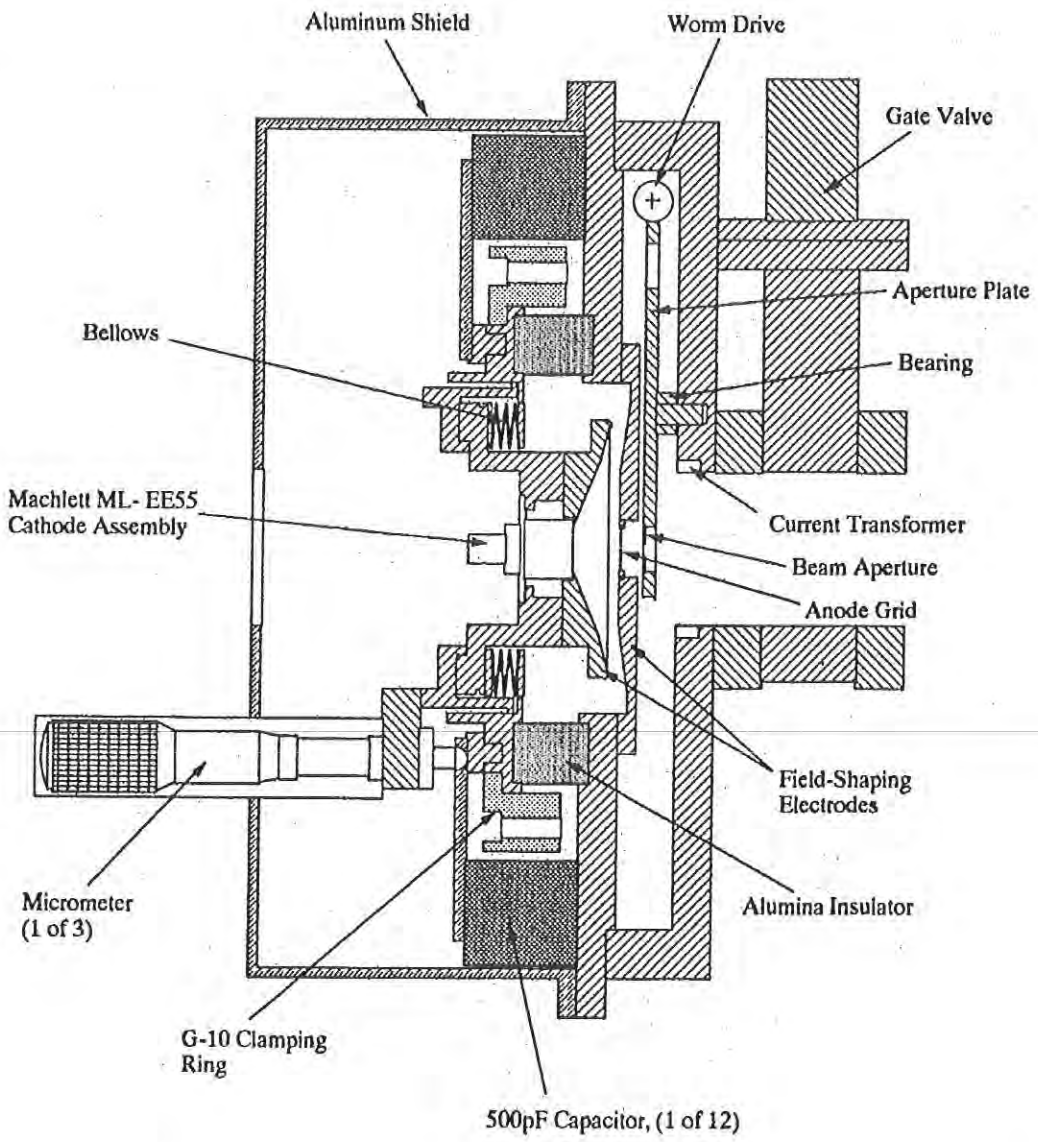

Figure 3.1. Schematics of gridded electron gun

with titanium. The grid-cathode spacing is very small, about 0.11 mm. The focusing electrode is connected to the grid and both are at the same high electrical potential. The electrodes of the gun are a Pierce geometry to generate a rectilinear flow in a circular, solid electron beam. The whole cathode assembly is mounted to a support through bellows. The anode and the field-shaping electrodes form a Pierce geometry. The distance between the cathode and anode is accurately adjustable between 9.3 mm and 23 mm, which results in a change in gun perveance. The 1cm diameter anode aperture is covered with a molybdenum mesh to reduce defocusing effects. The screening factor of the mesh is 14.3 %. An aperture plate is located downstream of the anode hole for the purpose of beam profiling and diagnostics. The distance between the anode wire mesh and the aperture plate is 1cm. The aperture includes eight circular holes with monotonically increasing diameters, one pepper-pot, one slit, and two multiple-beamlet configuration (see Table 3.1). A built-in fast current transformer (Rogowski Coil) is located after the aperture plate to measure the beam current. This gun also has a gate valve to isolate the cathode from the rest of the system. The gate valve is only open during experiments, while at other times or during system installation, the gate valve is closed to protect the cathode.

Aperture plate	Size Description	Typical Image	Beam Current For 5keV	Perveance K	Coder Number
Full size aperture	ϕ=12.5 mm (Full beam passes)		I=135 mA	5.78×10^{-3}	999993
Pepper-pot	ϕ=0.2 mm on a 1×1 mm^2 grid pattern	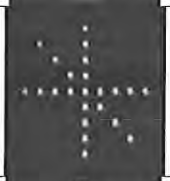	I=0.05 mA	2.14×10^{-6}	43
Slit	Length=8 mm Width=1 mm		I=12 mA	5.14×10^{-4}	93
Multi-beam1	ϕ1=2.88 mm ϕ2=0.2 mm D=4mm(center to center)	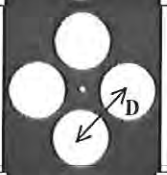	I_1=10 mA I_2=0.05 mA	4.29×10^{-4} 2.14×10^{-6}	143
Multi-beam2	ϕ1=5.7 mm ϕ2=0.8 mm D=5mm(center to center)	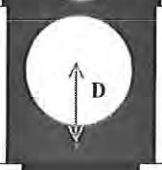	I_1=39 mA I_2=0.7 mA	1.67×10^{-3} 3×10^{-5}	193
Hole 1	ϕ=0.8 mm		I=0.7 mA	3×10^{-5}	243
Hole 2	ϕ=3.2 mm		I=12 mA	5.14×10^{-4}	293
Hole 3	ϕ=4.6 mm	…	I=25 mA	1.07×10^{-3}	343
Hole 4	ϕ=5.6 mm	…	I=37 mA	1.59×10^{-3}	393
Hole 5	ϕ=6.6 mm	…	I=52 mA	2.23×10^{-3}	443
Hole 6	ϕ=7.4 mm	…	I=65 mA	2.79×10^{-3}	493
Hole 7	ϕ=8 mm	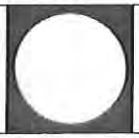	I=76 mA	3.26×10^{-3}	
Hole 8	ϕ=8 mm	Without aperture	No current		545

Table 3.1. Aperture plate description when A-K gap is 17mm for 5 keV beam

3.3 Gun Electronics

The gun electronics consist of a high voltage supply for the anode grid, an AC power supply for the cathode heater, a DC cathode-grid bias supply (in the experiment, it is 30 V to suppress the beam), and a grid-cathode pulser which provides a fast pulse signal between the cathode and grid to create the beam pulse. This pulser is triggered by an external triggering circuit. Figure 3.2 shows the circuit diagram for the electron gun [6]. High voltage is applied to the anode grid through a 1 MΩ resistor, which protects the high voltage power supply from damage in the event of a large discharge when the power supply turns off. All the electronics are located in a high voltage deck, which is isolated from the ground and charged up to –10 kV, except for the external triggering circuit, which is at the low voltage and has a connection to the high voltage electronics via fiber optics and an insulated transformer. The cathode is biased by positive DC voltage (30 V) relative to the grid to cut off the beam current. During emission, the grid-cathode pulse generator produces a negative pulse (-60 V) between the cathode and the grid to turn on the beam. The pulser signal is formed with a transmission line and the length of the transmission line determines the beam pulse width. The transmission line length is variable to produce different beam pulse lengths, and when the length of the transmission line is about 10 m, the pulse width is 100 ns. When the DC charging voltage is above -130 V(in the experiment, it is -160 V), the transistor works in the avalanche state. The avalanche transistor is turned on with the external

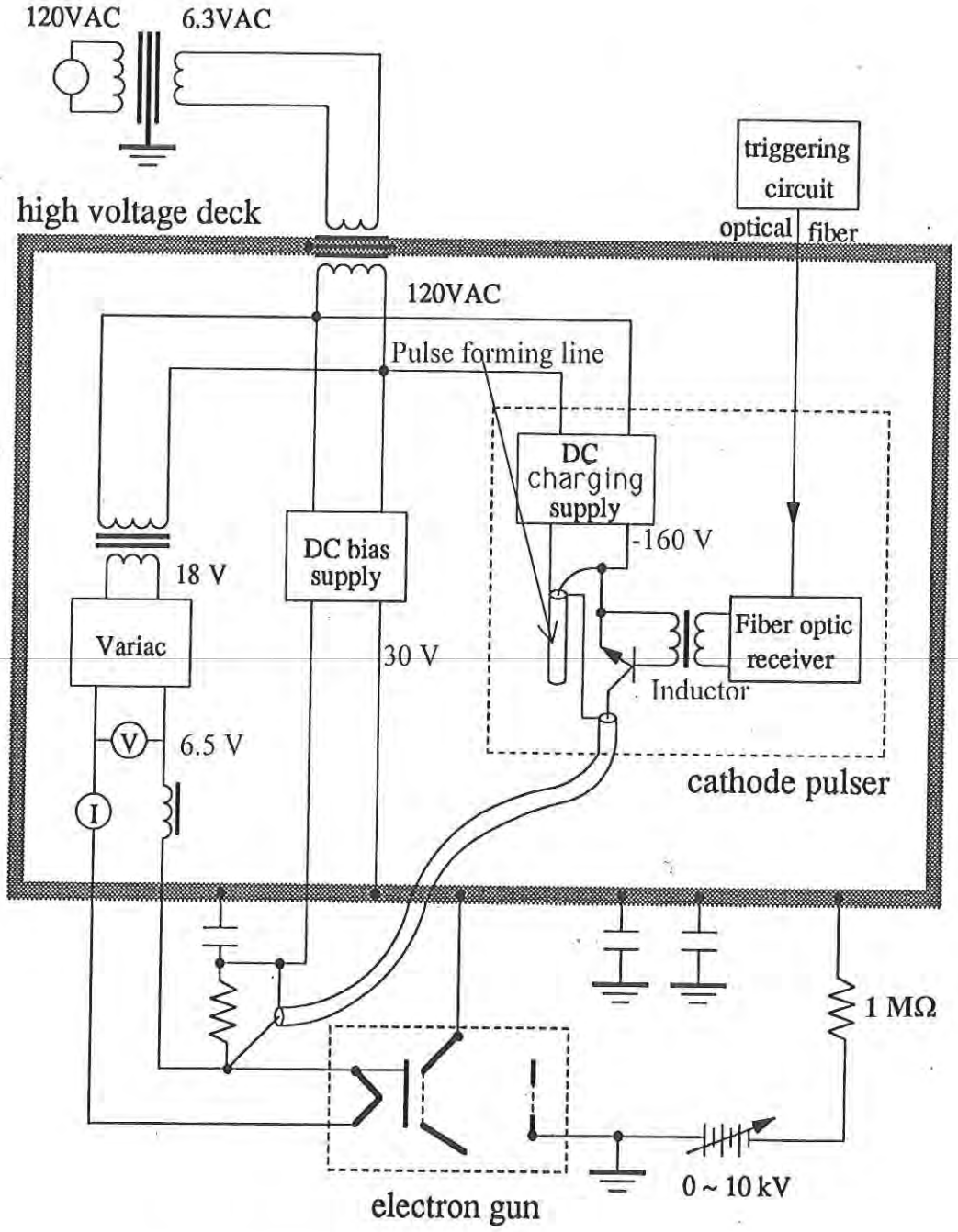

Figure 3.2 The Circuit diagram for electron gun

triggering circuit. A typical grid-cathode pulser signal is shown in Figure 3.3 and the pulser amplitude is above 60 V. Figure 3.4 is the pulser signal with a perturbation introduced by a T type connector. Figure 3.5 is the pulser signal with a perturbation introduced intentionally by a transmission line with a length of one foot. To save the cathode lifetime, the external trigger is run at 60 Hz. To avoid harmful effect from the magnetic field produced by the heating current, synchronization must be made between the pulse and the AC line voltage such that the beam is emitted when the line voltage is at the zero crossing.

For experimental reasons we relocated the electron gun to a new place, the new cables were changed in the high voltage deck, and the low voltage pulse generator circuit was packaged to make the electronics system of the gun safe and reliable.

3.4 Explanation of Pulser Tail and Experimental Improvement

In Figure 3.3, Figure 3.4, and Figure 3.5, I found that the pulser signal has a strange tail. When a perturbation is introduced into the pulser signal, the perturbation also appears on the tail. Since the pulser signal generates the beam pulse, we would like to remove the tail to get a better-shaped beam pulse.

The process forming the pulser signal is very complicated because there are a lot of factors affecting the shape of the pulser signal, such as the frequency characteristic of the transmission line, mismatched impedance between the connectors, DC charging voltage (-160 V), and the transistor avalanche effect, etc.

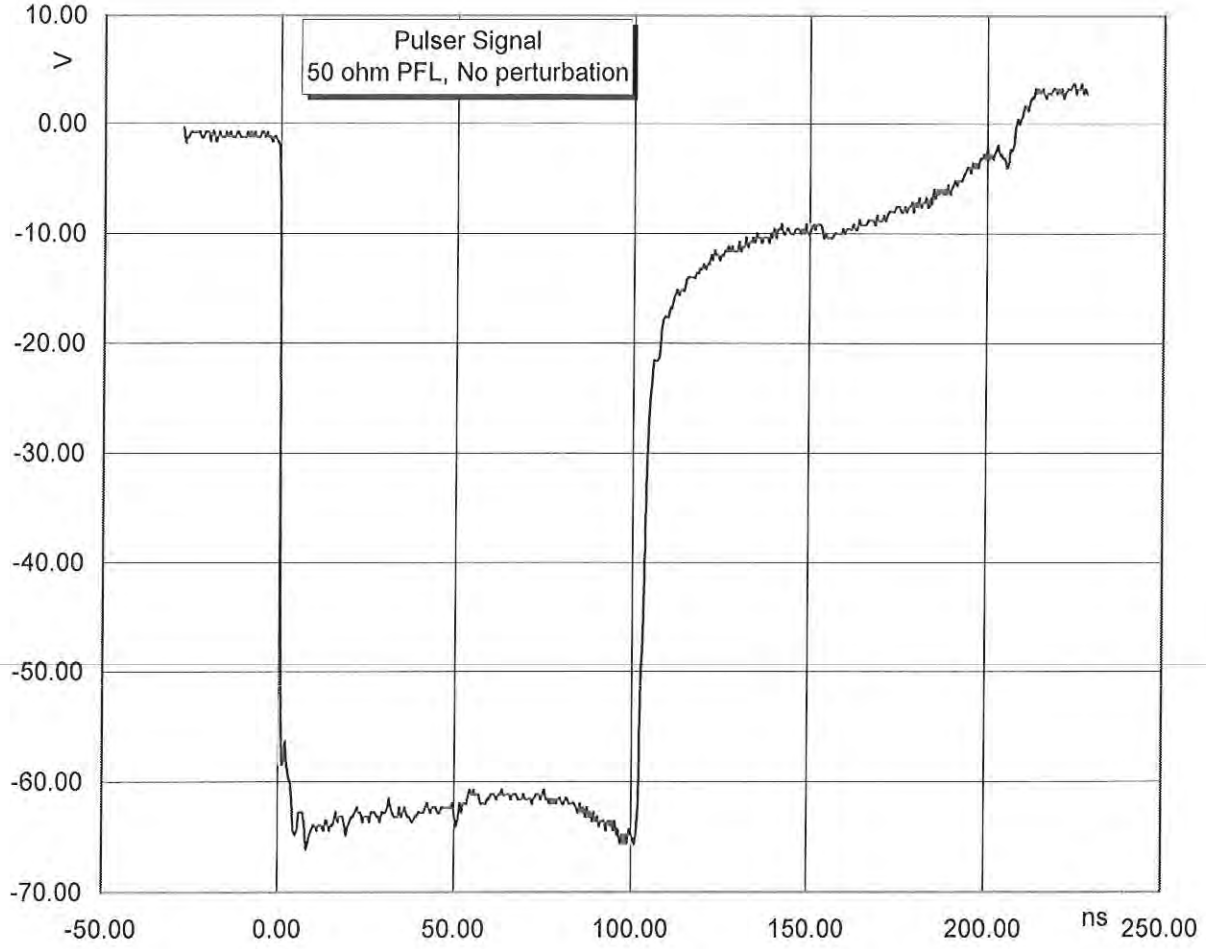

Figure 3. 3 Typical grid-cathode pulse in the electron gun.

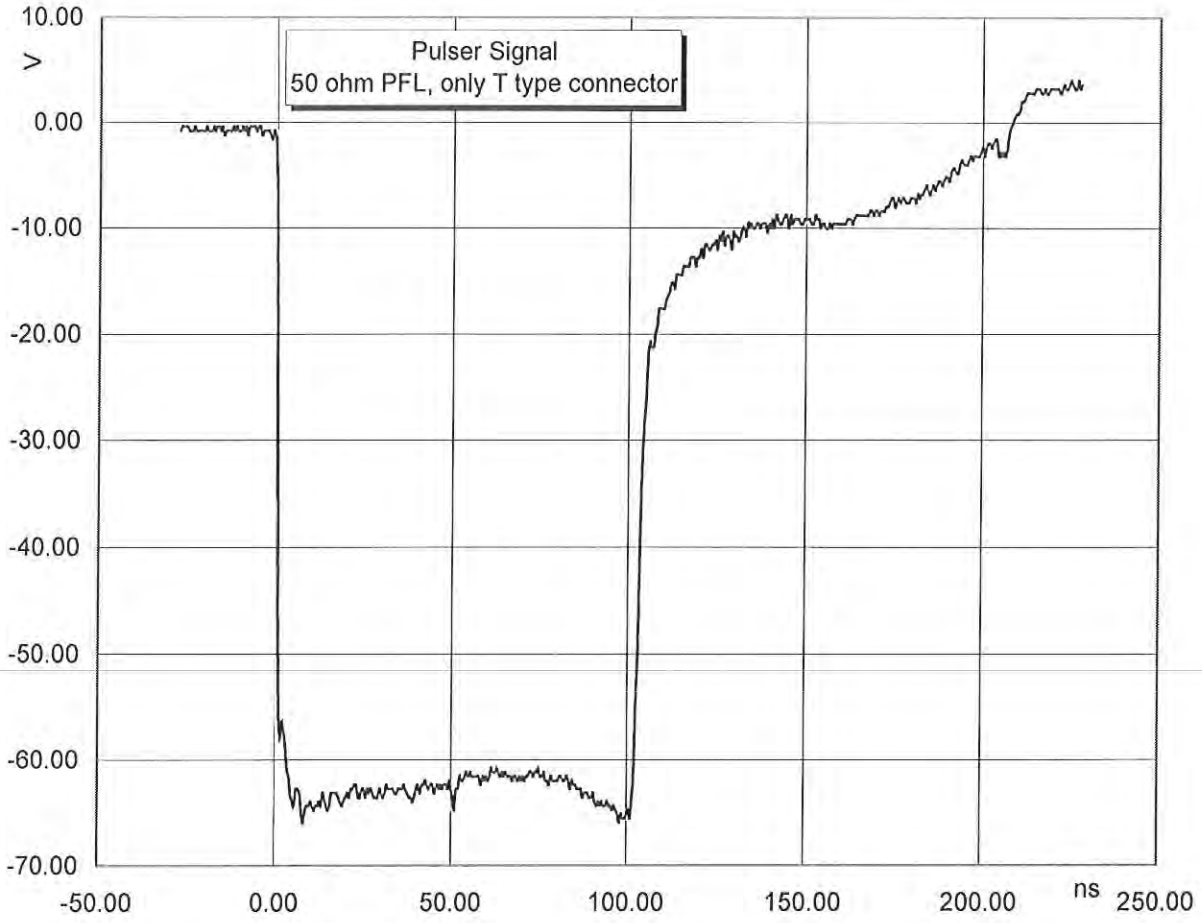

Figure 3.4 Grid-cathode pulse in the electron gun, the small bump in the middle is the perturbation caused by the T type connector

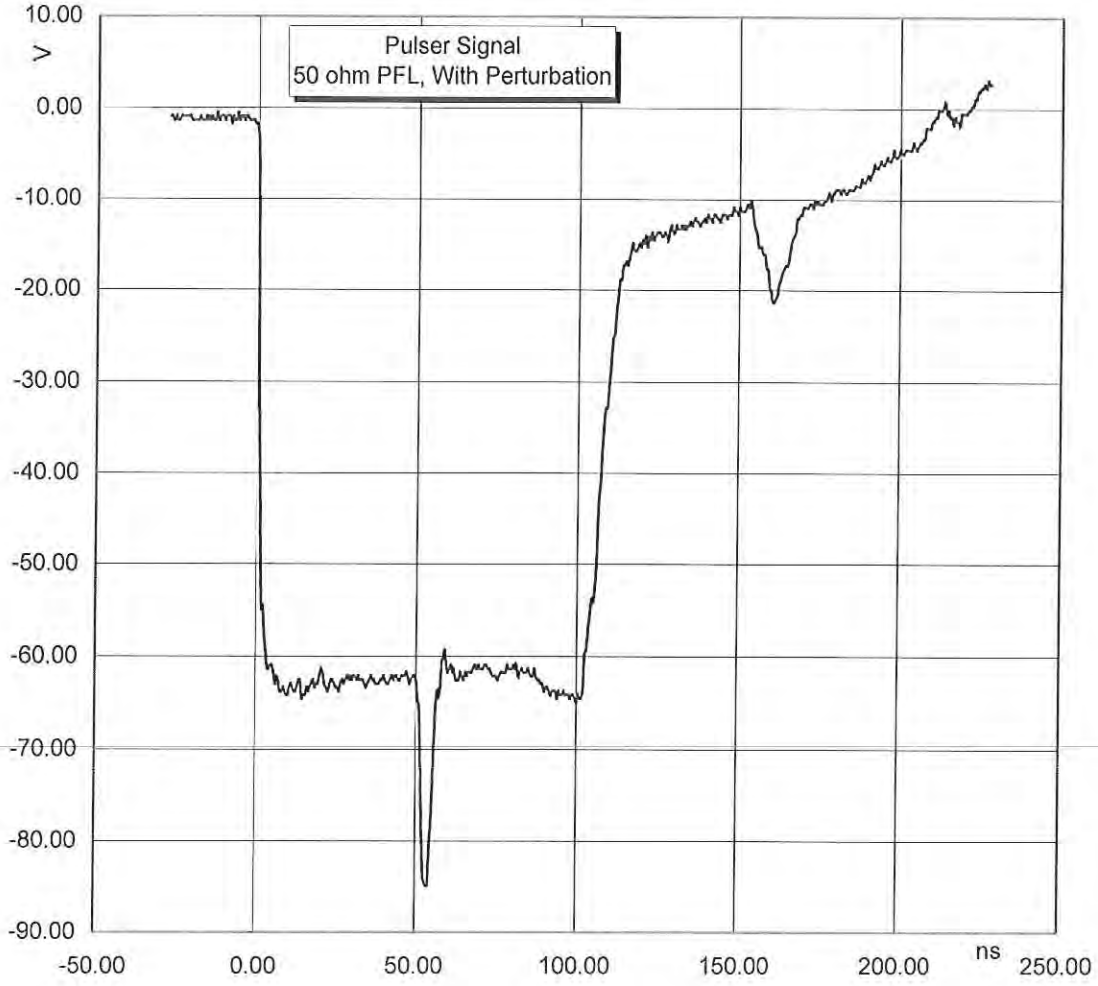

Figure 3. 5 Grid-cathode pulse. The bump in the middle is the perturbation introduced by a transmission line with a length of one foot

At the beginning, I suspected the frequency characteristics weren't good and there was a large attenuation in the pulse forming line. But after the frequency characteristics of the pulse forming line were measured, I found the attenuation is very small and it can be neglected when I do analysis.

The reflection wave theory is used to analyze how the pulser signals are formed in Figure 3.3-3.5. In Figure 3.2, when there is no high frequency triggering signal on the transistor, the voltage between the base and emitter of the transistor is zero and the transistor is closed [9]. When an external triggering pulse arrives, voltage difference between the base and emitter generated by the inductor will makes the avalanche channel open between the collector and emitter because the voltage of 160 V between the collector and emitter is large enough to let the transistor avalanches. There is an instant big current signal from collector to emitter to form a quick pulse drop at the emitter of the transistor. It will be like an incident wave traveling along the transmission line and will be completely reflected back to the emitter of the transistor in a fixed time because the transmission line is open at the terminal [10,11,12]. We used 50 Ω RG58A/U coaxial cable as the pulse forming line. The length of the transmission line is about 10 m and the reflected wave will have a delay of 100 ns.

Figure 3.6 shows the detailed pulser circuit schematics. The characteristic impedance Z_l of the pulse forming line is 50 Ω. At the emitter of the transistor, a current pulse drop, incident wave (I_{il}) shown in Figure 3.7 (a), enters the pulse

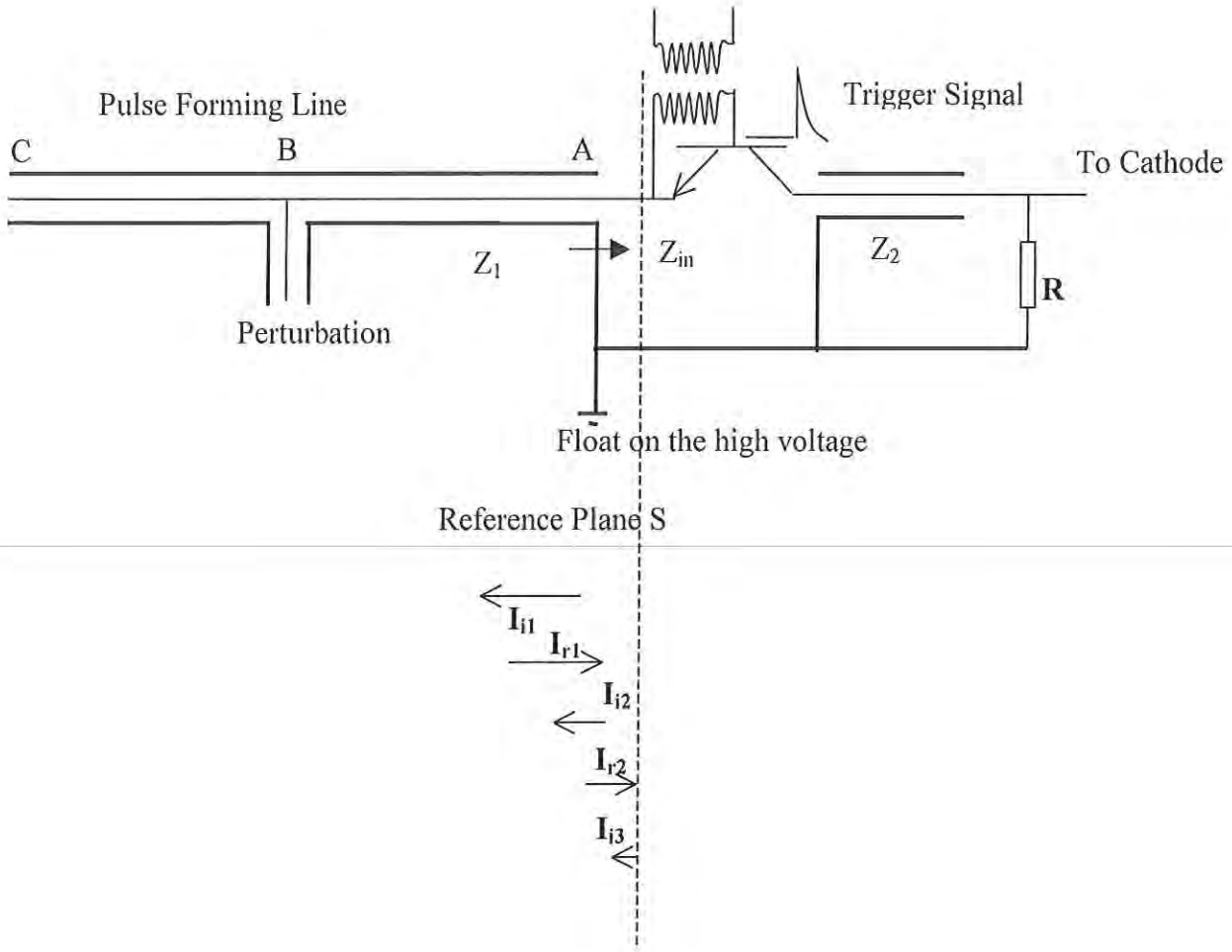

Figure 3.6 Pulser Circuit Schematics

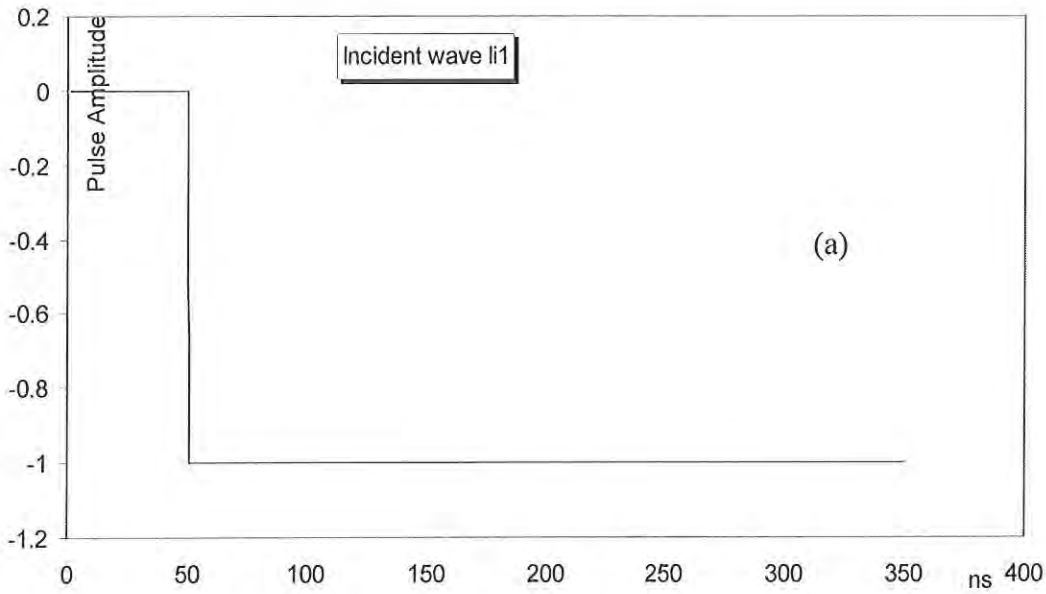

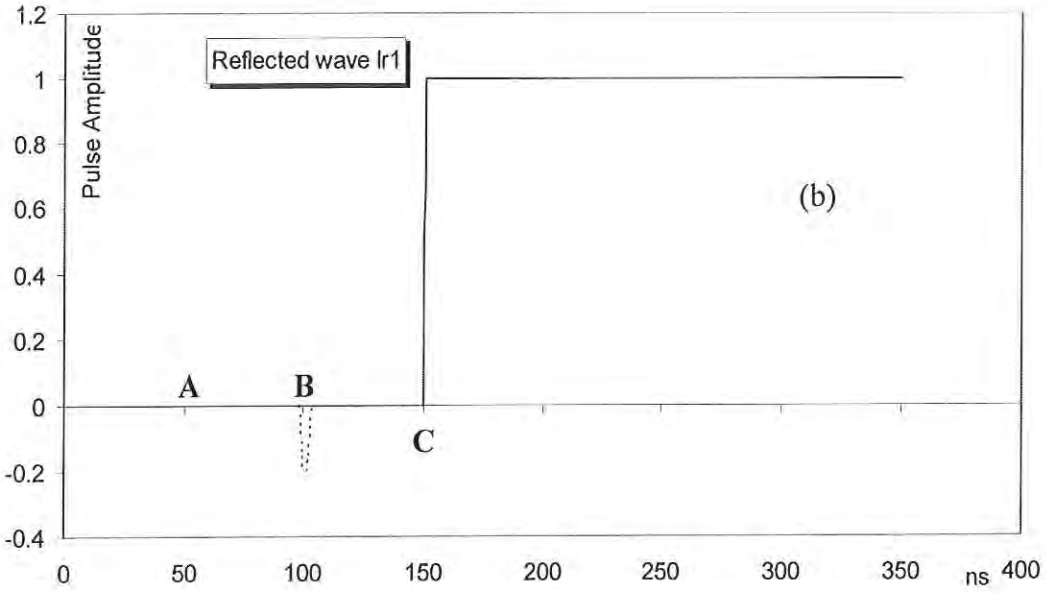

Figure 3.7 Pulser signal forming process (a)Incident wave (I_{i1})
(b)Reflected wave I_{r1}

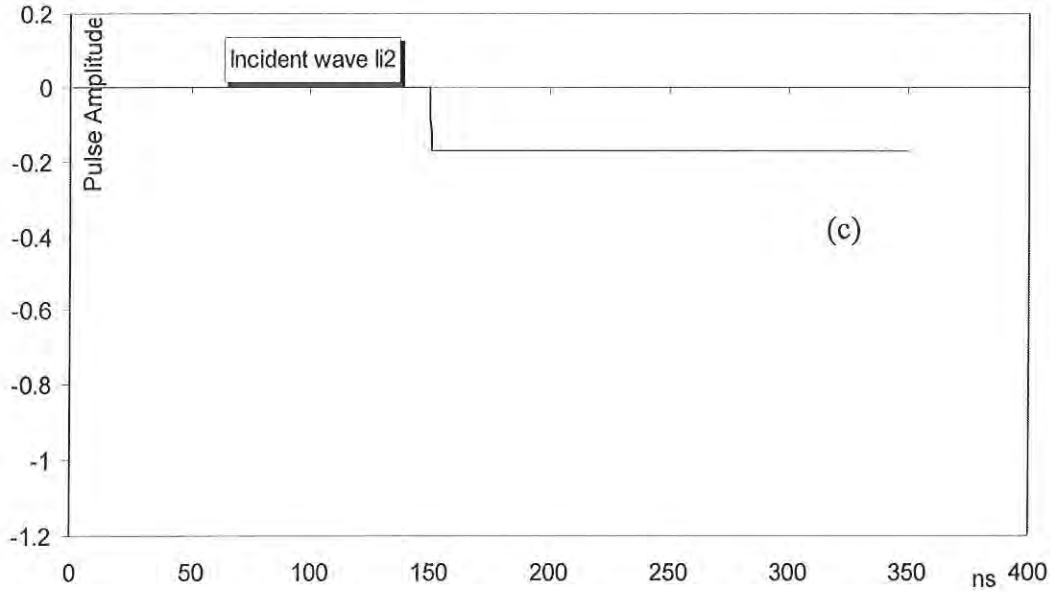

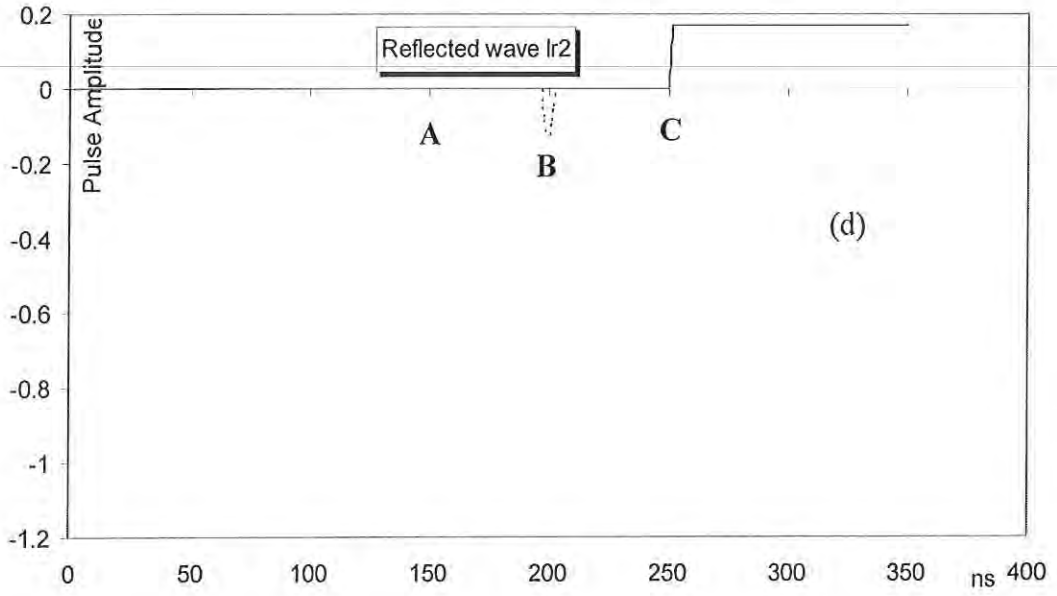

Figure 3.7 Pulser signal forming process (c)Incident wave (I_{i2})
(d)Reflected wave (I_{r2})

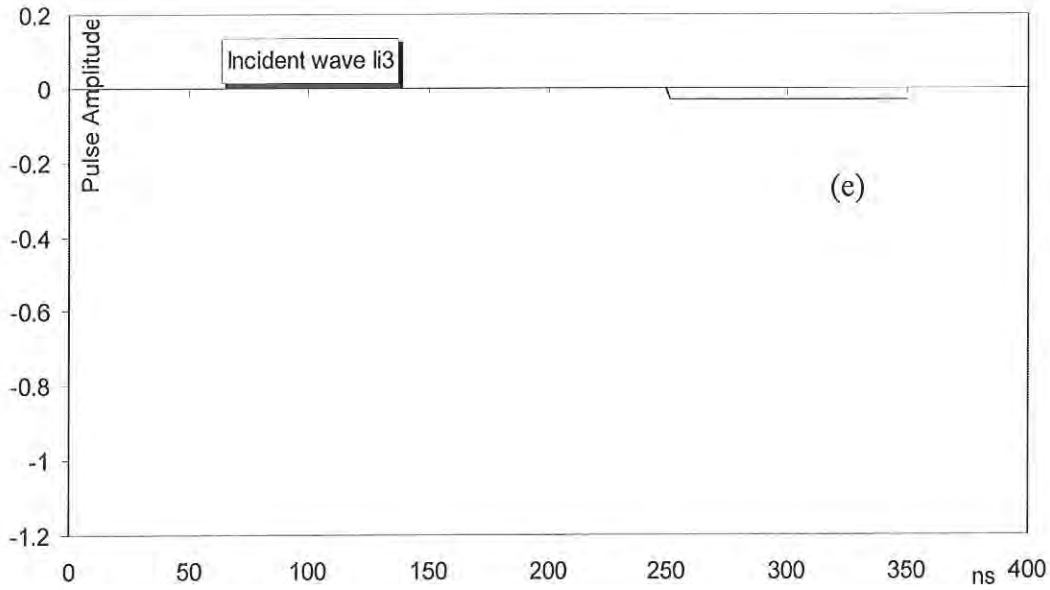

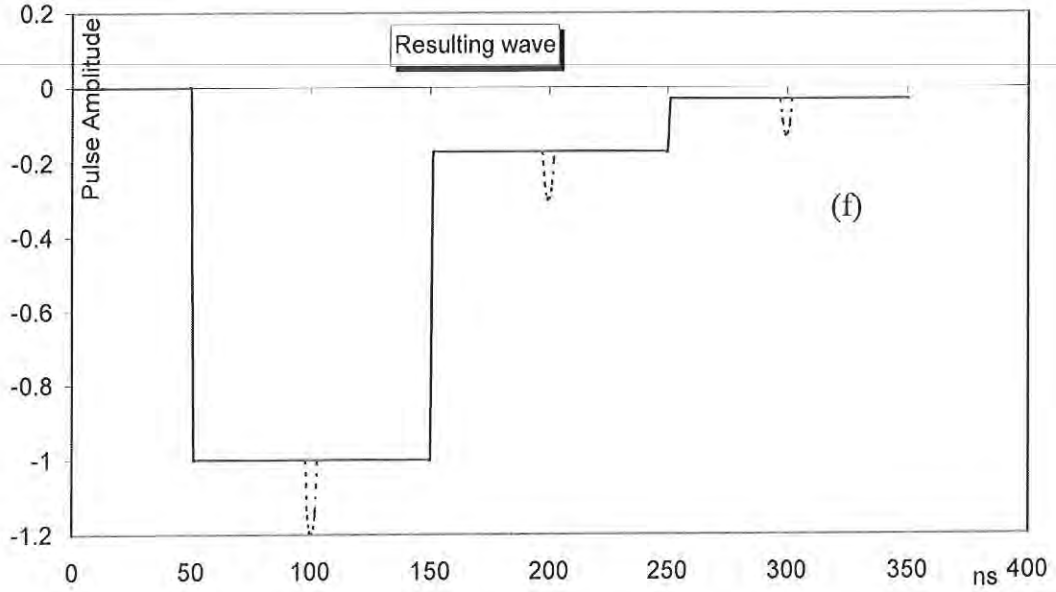

Figure 3.7 Pulser forming process (e)Incident wave (I_{i3})
(f) Resulting wave after all incident waves and reflected waves superpose

forming line. Let us observe three points, A, B, and C, along the pulse forming line in the Figure 3.6. Point A is the starting point of the transmission line, B is the middle point and C is the ending point. The incident wave is not reflected at the A and B for it is matched at these two points if no perturbation is introduced. When the incident wave reaches C, incident wave is completely reflected back to the emitter of the transistor after 100 ns because the transmission line is open at the C and its reflection coefficient is 1. The reflected wave (I_{r1}) shown in Figure 3.7(b) has a time delay, a reversed phase compared with the incident wave, and the same amplitude as the incident wave. If a perturbation is introduced at the B of the pulse forming line [13], when the incident wave reaches B, because the point B isn't completely matched, a small reflection is added into the reflected wave (I_{r1}). The additional dotted line shown in Figure 3.7 (b) is the perturbation introduced intentionally.

When the reflected wave (I_{r1}) goes back to the emitter of the transistor, because the input impedance of the emitter isn't completely matched to the pulse forming line, an incomplete reflection happens at the emitter. Part of the reflected wave (I_{r1}) is reflected by the emitter and forms the second incident wave (I_{i2}) shown in Figure 3.7 (c). The study about the avalanche characteristics of the transistor is very little. The theoretical input impedance of the emitter is difficult to get, but it can be determined by experiment. From experiment results in Figure 3.3-

3.5, we know the amplitude of the I_{i2} is about 17 % of the reflected wave (I_{r1}). The reflection coefficient Γ looking into the emitter at the reference plane S:

$$\Gamma = \frac{Z_{in} - Z_1}{Z_{in} + Z_1} = \frac{I_{i2}}{I_{r1}} = 17\% \qquad (3.1)$$

where Z_{in} is the emitter equivalent input resistance seen and Z_1 is the characteristic impedance of the pulse forming line, 50 Ω.

According to equation (3.1), the input resistance of the emitter, Z_{in}, is about 70 Ω. It is mismatched to the 50 Ω pulse forming line.

The incident wave (I_{i2}) enters the pulse forming line, repeats the same process as incident wave (I_{i1}). Then we have the reflected wave (I_{r2}) in Figure 3.7 (d) produced by pulse forming line and the third incident wave (I_{i3}) in Figure 3.7 (e) reflected by the emitter. The incident wave (I_{i3}) is very small, about 2 percent of the pulser signal if the reflection coefficient is 17 % at the emitter. Such a small signal can be ignored.

After all incident waves and reflected waves superpose, the resulting wave is shown in Figure 3.7 (f). The pulser signal we observe is the resulting wave. Figure 3.7 (f) is very similar to the experiment result shown in Figure 3.3-3.5 including the situation with perturbation. So reflection due to input impedance of the transistor mismatched to the pulse forming line causes pulser signal tail. The experimental result of the pulser tail gradually attenuates because the avalanche

channel of the transistor trends close when the current between the collector and the emitter is smaller at the pulser tail.

To check whether the explanation is right, I need to match the emitter input impedance to the pulse forming line. I can't change the input impedance of the avalanche transistor, but I can change the pulse forming line. A 75 Ω RG 59/U coaxial cable with a length of 10m, whose characteristic impedance is close to the emitter input resistance 70 Ω, replaces the 50 Ω RG 58A/U coaxial cable as pulse forming line. I found the pulse signal tail is reduced greatly because the reflection at the emitter is very small. The experiment results are shown in Figure 3.8 without perturbation and Figure 3.9 with perturbation. When the pusler signal finishes, it almost recovers to zero and has no tail exists. This signal is acceptable because some very small ripple doesn't affect the beam emission.

The pulser output signal from the collector of the transistor to cathode still uses 50 Ω transmission line (Z_2 in Figure 3.6). The reasons are as follows: 1. The terminal of 50 Ω transmission line is 50 Ω matched load at the cathode. We don't need to worry about reflection. 2. The pulser output signal often need to be checked connecting to the oscilloscope. The oscilloscope has a 50 Ω input impedance, but no 75 Ω input impedance. The pulser signal needs to match oscilloscope.

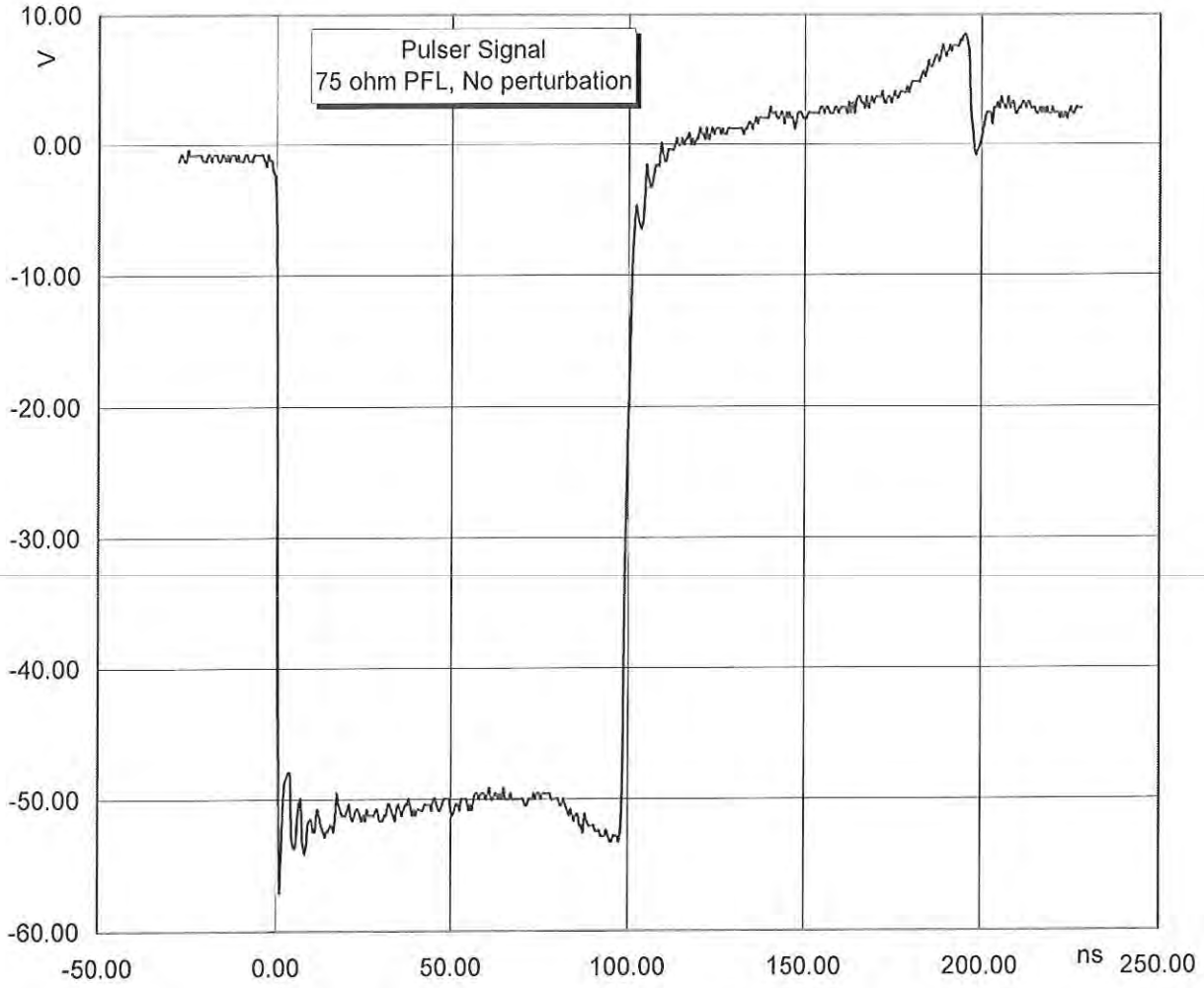

Figure 3.8 Pulser Signal Using 75 Ω Pulse Forming Line, no Perturbation

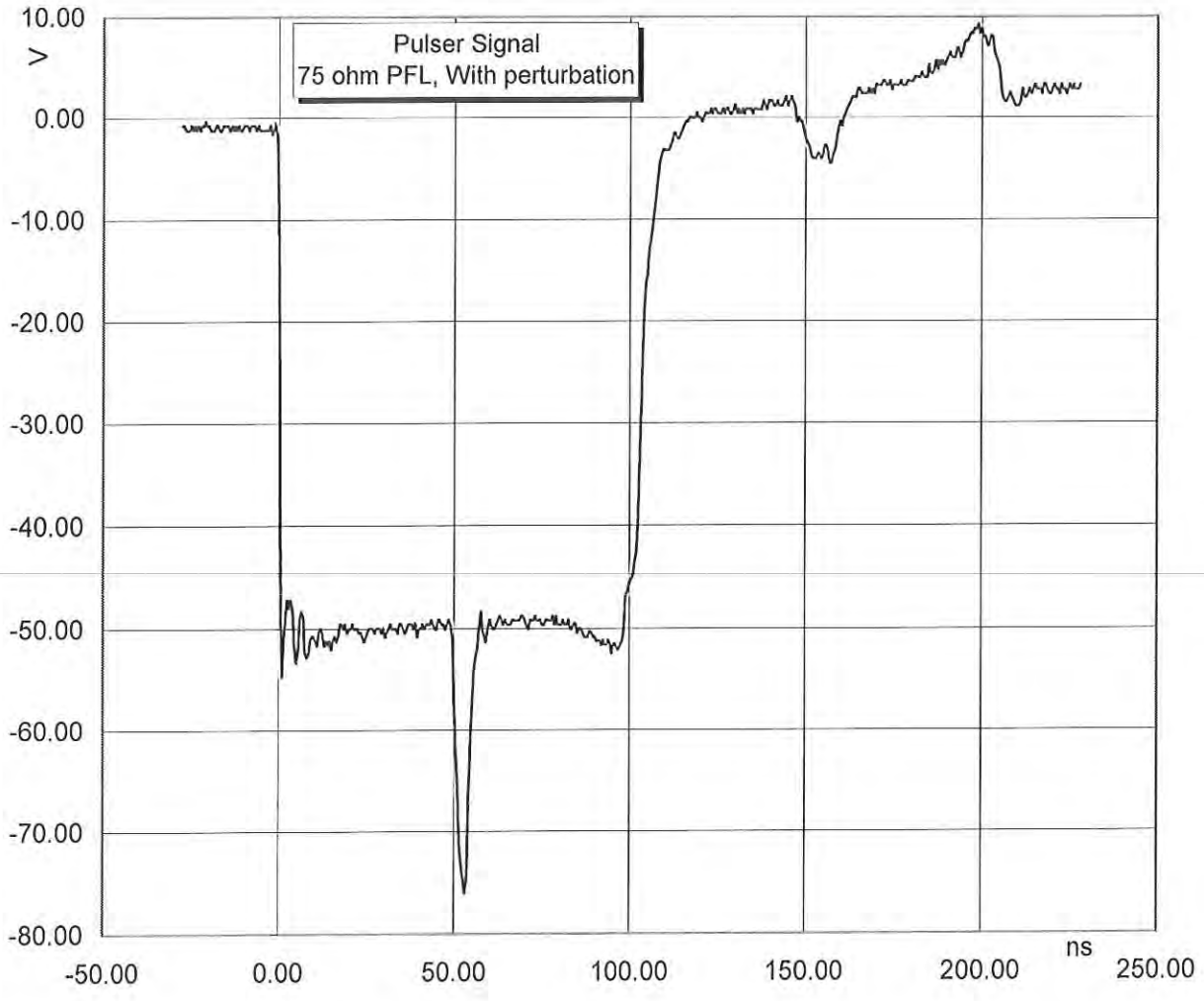

Figure 3.9 Pulser Signal Using 75Ω Pulse Forming Line, with Perturbation

We also tested the pulser signal of the UMER gun. Figure 3.10 shows the experimental results of the pulser signal using the 50 Ω pulse forming line. After the 75 Ω pulse forming line was used, we got much better pulser signal shown in Figure 3.11. Two overshot signals in Figure 3.11 are caused by mismatched connectors.

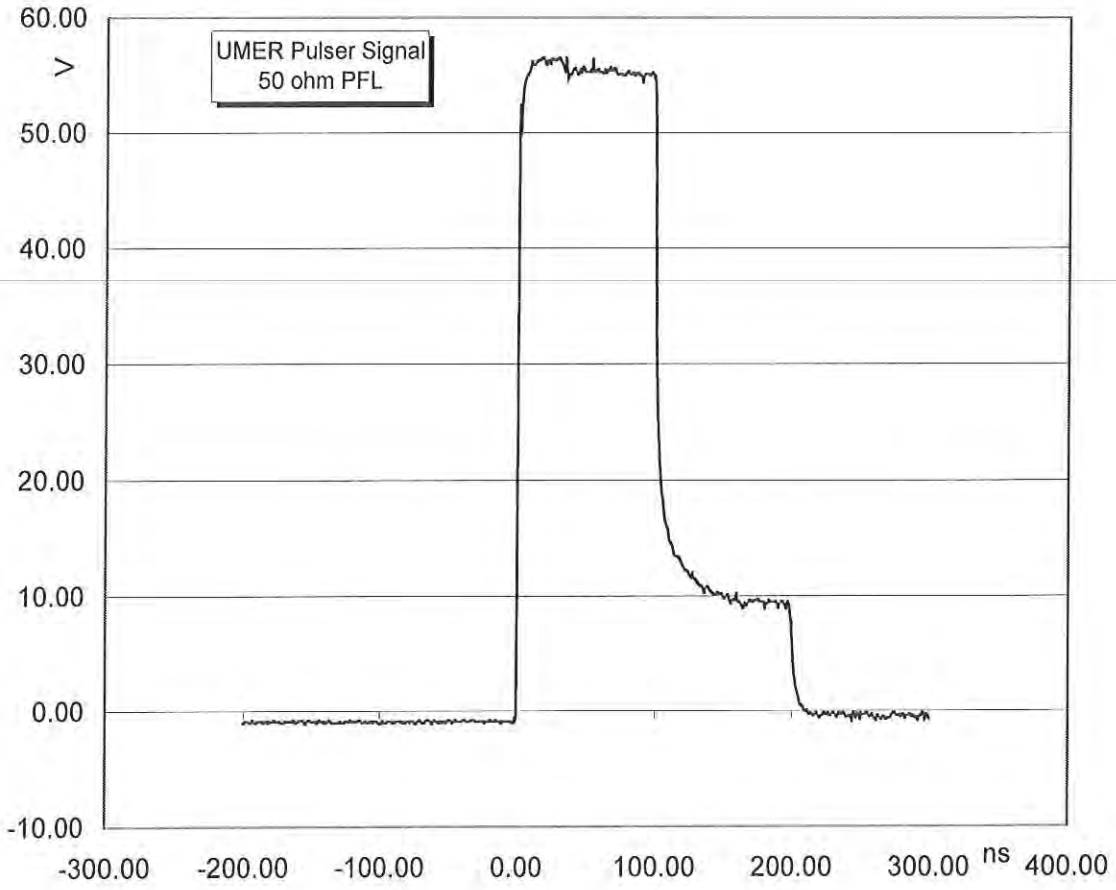

Figure 3.10 UMER Pulser Signal Using 50 Ω Pulse Forming Line

No Perturbation

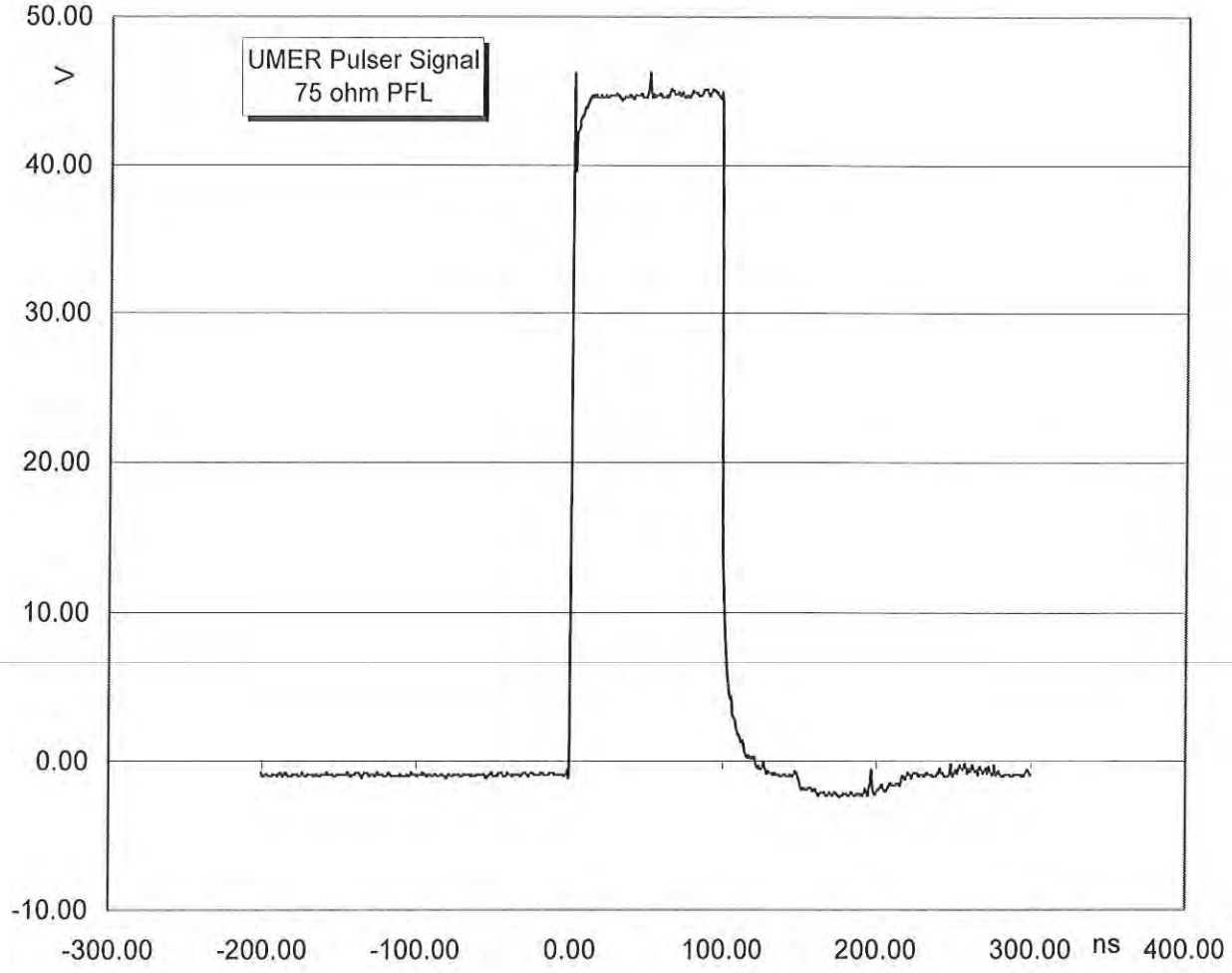

Figure 3.11 UMER Pulser Signal Using 75 Ω Pulse Forming Line

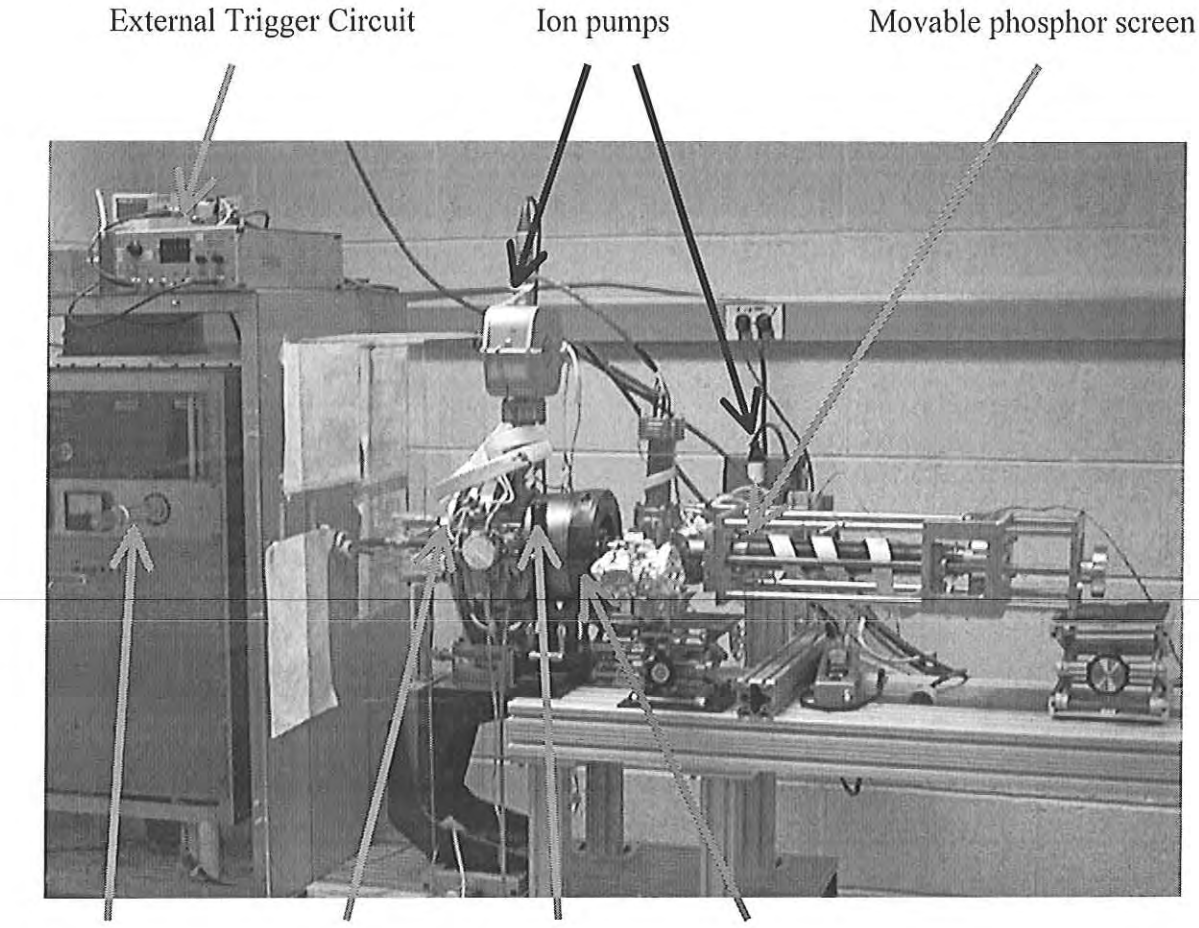

Figure 3.12 Set up for measuring Initial Condition of Electron gun

3.5 Gun Performance and Beam Initial Condition

The experimental set up shown in Figure 3.12, which includes a focusing solenoid, current monitor, and movable phosphor screen, is to measure gun's performance and the initial condition of the beam. The current monitor can measure beam current and the movable phosphor screen can measure the beam image along the z-axis. In this experiment, the vacuum is kept at low 10^{-8} Torr. Higher vacuum can result in better gun emission and longer cathode lifetime.

3.5.1 Beam current versus heating voltage

The relation of beam current versus heating voltage is shown in Figure 3.13 for different high voltage levels. Other parameters include an A-K gap of 17 mm, a grid-cathode bias of 30 V, and a DC charging voltage of 160 V. The cathode could be heated from room temperature to the working condition in about an hour when the heating voltage is increased 0.5 V per 5 mins. The working heating voltage is around 6.5 V and the heating current is about 1.4 A, which yields a heating power of 4.5 W. At this heating voltage, the beam current is steady for different high voltage levels. If the temperature is too high, too much material will be evaporated and if the temperature is too low, the emission is decreased [6,8].

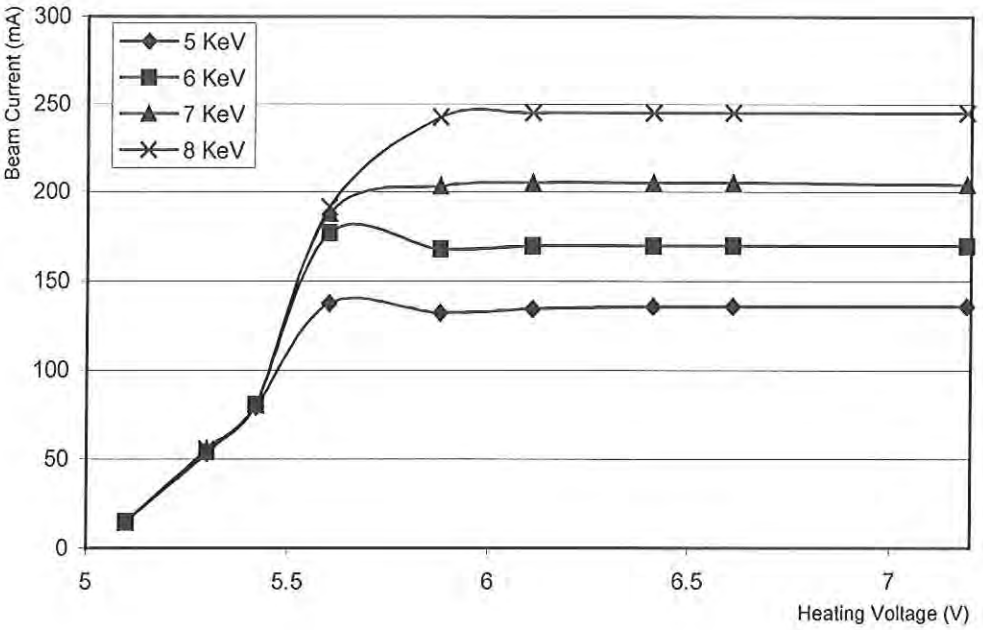

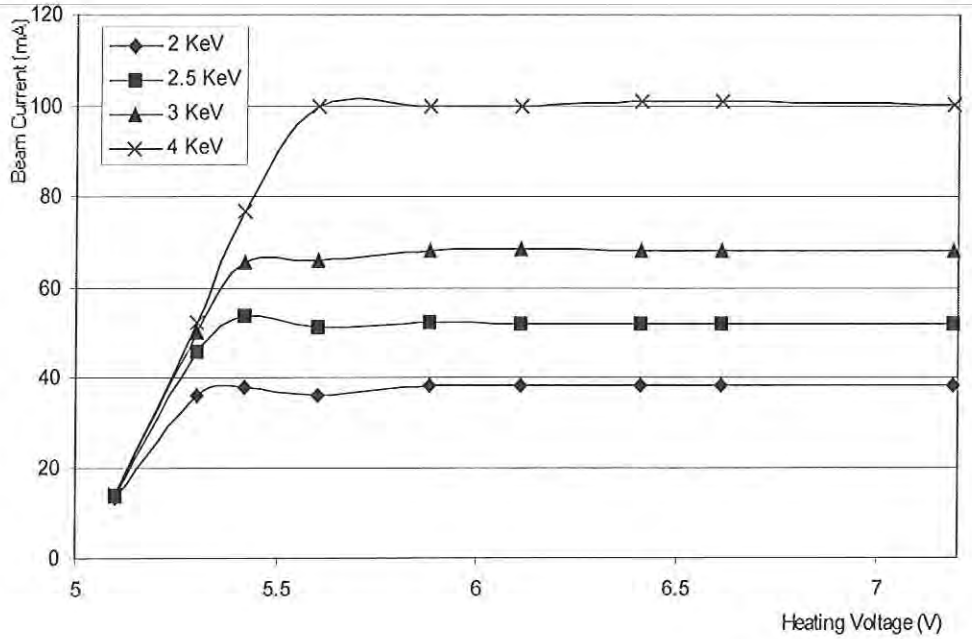

Figure 3.13 Beam Current versus the heating voltage for fixed A-K gap 17 mm at different high voltage level

3.5.2 Beam current versus anode-grid high voltage

The relation of beam current versus anode-grid high voltage is shown in Figure 3.14. This measurement is performed at the following conditions: an A-K gap of 17 mm, a grid-cathode bias of 30 V, a DC charging voltage of 160 V, and a fixed heating voltage of 6.5 V and heating current of 1.4 A. For a planar electrode geometry with a gap distance d, the current density is given by Child's law [1]:

$$J = 1.67 \times 10^{-3} \left(\frac{q}{mc^2}\right)^{1/2} \frac{V_0^{3/2}}{d^2} \qquad [A/m^2] \qquad (3.2)$$

Applying this result to a uniform round beam with a radius R, the beam current before the anode mesh is:

$$I = 1.67 \times 10^{-3} \pi \left(\frac{q}{mc^2}\right)^{1/2} V_0^{\frac{3}{2}} \left(\frac{R}{d}\right)^2 \qquad [A] \qquad (3.3)$$

In the figure, the data points are the beam current measured in the experiment and curve is the current derived from the Child's law after taking into account the anode screening effect on the beam current from the anode wire mesh. The beam radius R is about 5 mm. When the anode-grid high voltage is small, or the beam current is low, the measured beam current agrees very well with the theory. At large anode-grid high voltages, there is a tendency for the beam current to saturate as the grid-cathode potential remains fixed [6].

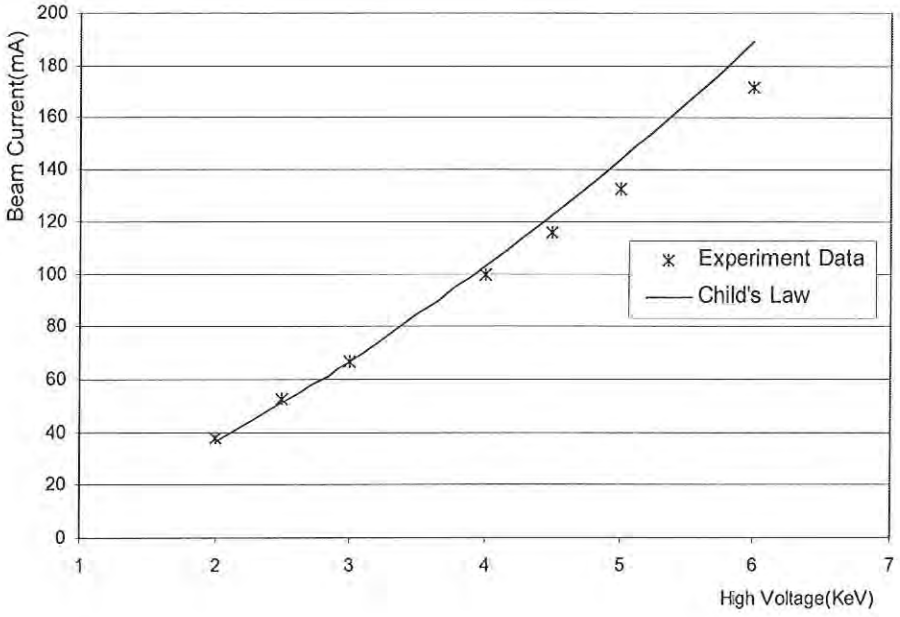

(a)

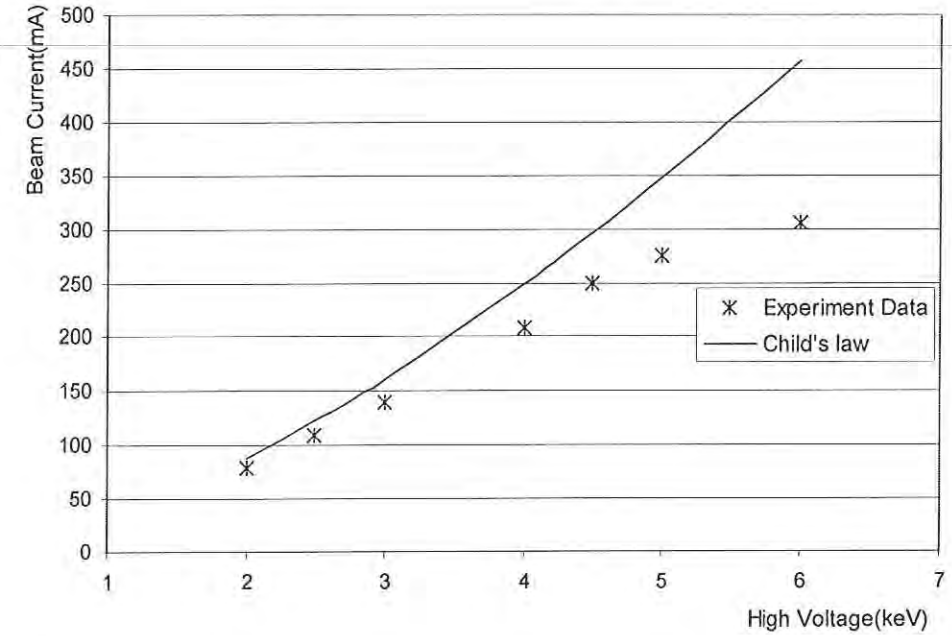

(b)

Figure 3.14 Beam current versus anode-grid voltage where the stars are the current measured and smooth curve is from Child's law. In Figure (a) A-K gap is 17 mm and in Figure (b) A-K gap is 11 mm

3.5.3 Beam current versus A-K gap

Figure 3.15(a) shows experimental results for beam current versus A-K gap on different high voltage settings. Other parameters include: Grid-cathode bias of 30 V, DC charging voltage of 160 V, and fixed heater voltage of 6.5 V. Figure 3.15(b) shows that the relation of measured beam current versus the A-K gap for 3 keV beam agrees within the experimental error with that predicted by Child's law [1], which is represented by the smooth curve.

Changing the A-K gap at a fixed anode-grid voltage results in a variation of the perveance of the gun. For a non-relativistic electron beam, the generalized perveance K is given by [1]:

$$K = 1.515 \times 10^{-4} \frac{I}{V^{3/2}} \qquad (3.4)$$

The data in Figure 3.15 show the generalized perveance varies from 0.003-0.0135. For 5 keV, 135 mA beam, when A-K gap is 17 mm, the generalized perveance is 0.00578.

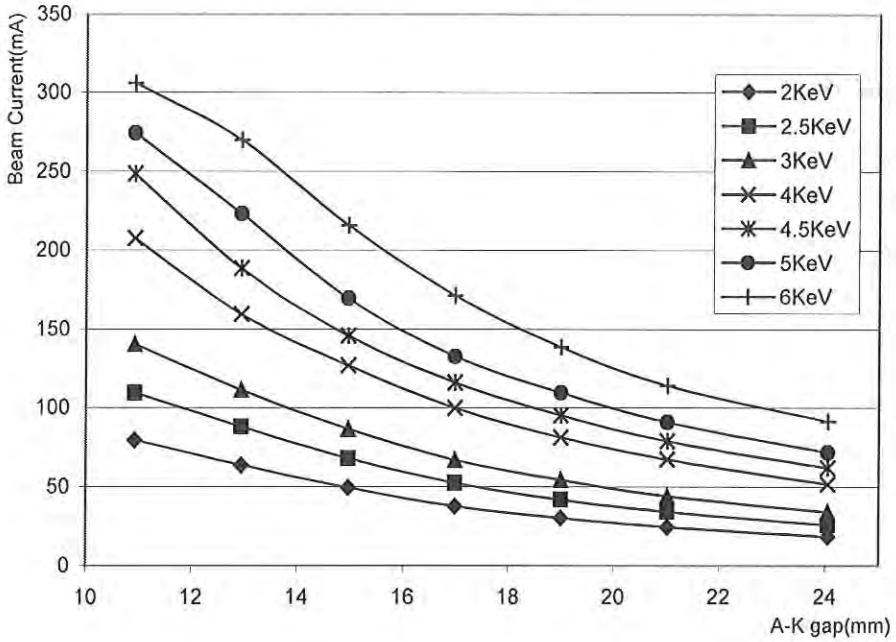

(a)

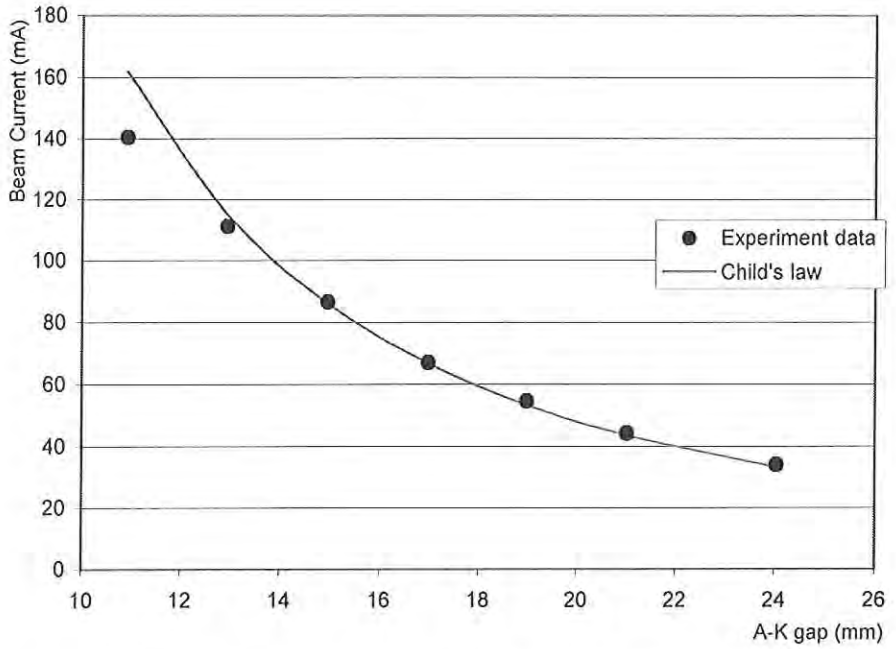

(b)

Figure 3.15(a) Beam Current versus A-K gap for different high voltage
Figure 3.15(b) Beam Current versus A-K gap for at 3 keV beam and smooth curve is generated from Child's law

3.5.4 Using pepper-pot to measure emittance

Emittance is a very important parameter to evaluate the beam quality. A pepper-pot in the position of the aperture of the gun is employed to measure the beam emittance. The phosphor screen system can be moved along the z-axis of the system from the aperture (Figure 3.12). Beam images on the phosphor screen are recorded by a camera.

The pepper-pot and a typical pepper-pot beam image have been introduced before in Table 3.1. Its holes are 0.2 mm in diameter and are drilled on a 1 mm by 1mm grid pattern. The pepper-pot holes are small enough that the beamlets formed by the pepper-pot are emittance dominated when expanding in a drift space. For example, the beamlet current becomes only 0.048 mA after a 5 keV beam passes the small hole, and the generalized perveance is 2×10^{-6}. The space charge effect will be very small.

The emittance can be calculated as follows. In Figure 3.16, a schematic drawing is shown for emittance measurement [6], where D and D_z are the size of the pepper-pot hole and its image on phosphor screen. S and S_z are the distances from the axis to the center of the pepper-pot hole and corresponding image; and z is the distance between the pepper-pot plate and the phosphor screen.

Assume the transverse density distribution of the full beam is uniform. The angular spread at any point in the beam is expressed as $x'=\varepsilon/R$, where ε is the beam emittance and R is beam waist radius. The image size contributed by the emittance

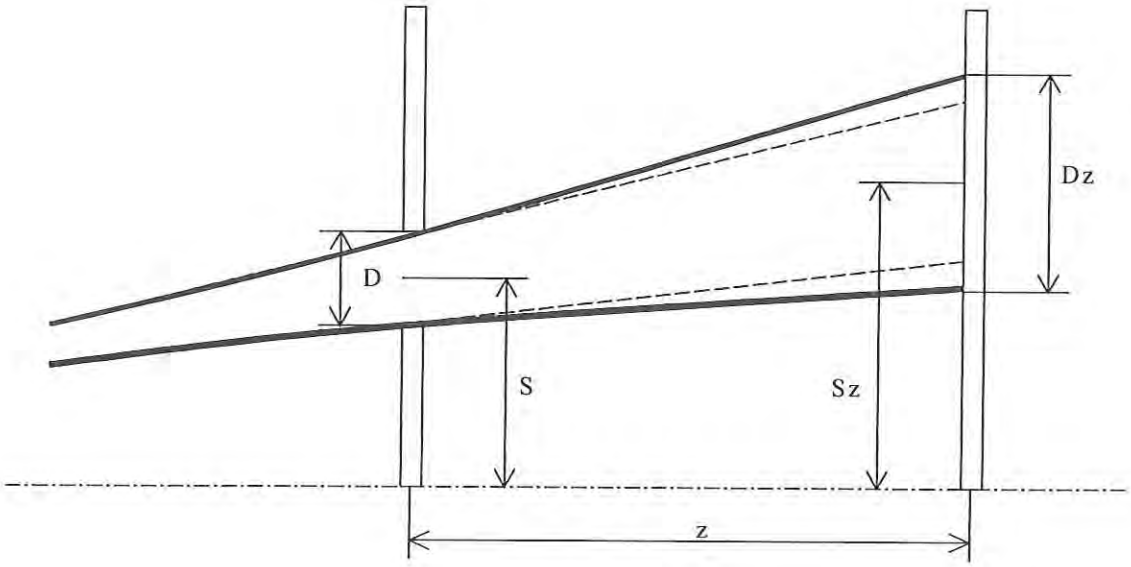

Figure 3.16 schematic drawing for Pepper-pot measurement

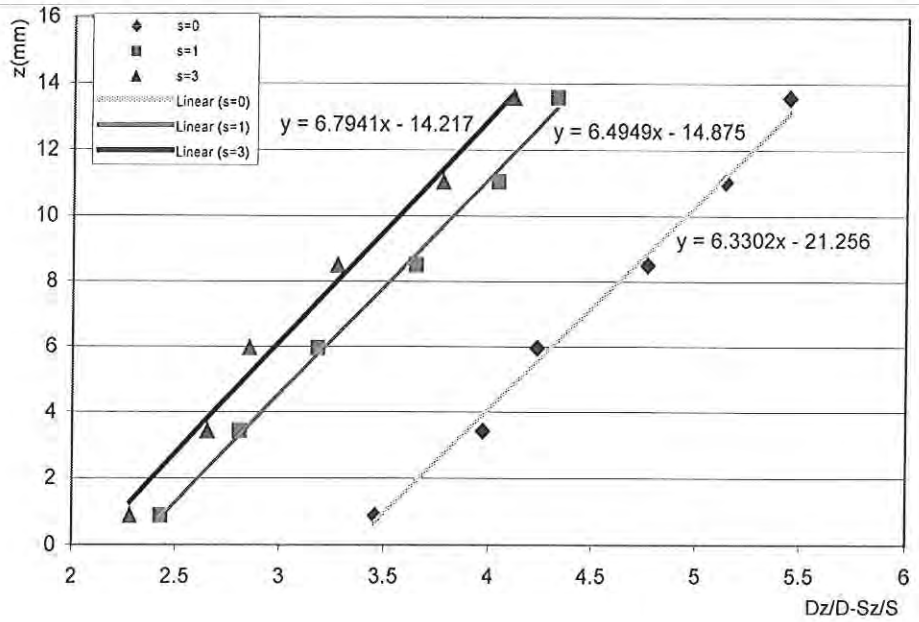

Figure 3.17 Pepper-pot measurement result for different distances of s=0, s=1 mm, and =3 mm from the axis.

is $2\varepsilon z/R$ with z being the distance between the pepper-pot plane and image plane.

The total image size is then $D_z = DS_z/S + 2\varepsilon z/R$, where the first term is geometric relation with a zero emittance beamlet [6].

$$\varepsilon = \frac{RD}{2z}\left(\frac{D_z}{D} - \frac{S_z}{S}\right) \tag{3.5}$$

In order to improve the accuracy of measurement, the pepper-pot images are taken at different distance z. Figure 3.17 shows the relation of $D_z/D\text{-}S_z/S$ versus z. The slope of the fitting line for the data point will be related to the emittance by

$$a = \frac{RD}{2\varepsilon} \tag{3.6}$$

For 5 keV, 135 mA beam, when the A-K gap is 17 mm, beam waist R is equal to 4.8 mm and emittances are in the range of 64-75 mm·mrad with an average of 72 mm·mrad and a standard deviation of 4 mm·mrad for eight pepper-pot image measurements.

3.5.5 Beam Initial Envelope

The beam envelope expansion in drift space is studied by the full beam image on the phosphor screen along the downstream of the beam starting from the aperture.

In Figure 3.18 data points show the beam radius [14] measured along the z-axis for 5 keV, 135 mA beam. The beam radius expands from 5.02 mm at the aperture to 9 mm at a location 6 cm from the aperture. This initial condition of the beam is necessary for beam matching and simulation.

The envelope equation for the expanding beam in the drift space is [1]

$$R_m'' - \frac{K}{R_m} - \frac{\varepsilon^2}{R_m^3} = 0, \qquad (3.7)$$

where R_m is beam radius, ε is the beam transverse emittance, and K is the generalized perveance. Using this equation and the beam initial condition, the computer code SPOT [15] gives the envelope curve shown in Figure 3.18, which is very close to the experimental result. In simulation, when emittance was set to zero, we found that the envelope of the beam changed very little. This shows the beam is space-charge dominated.

The beam initial condition was measured and will be very useful for matching the beam and calculating the energy spread evolution.

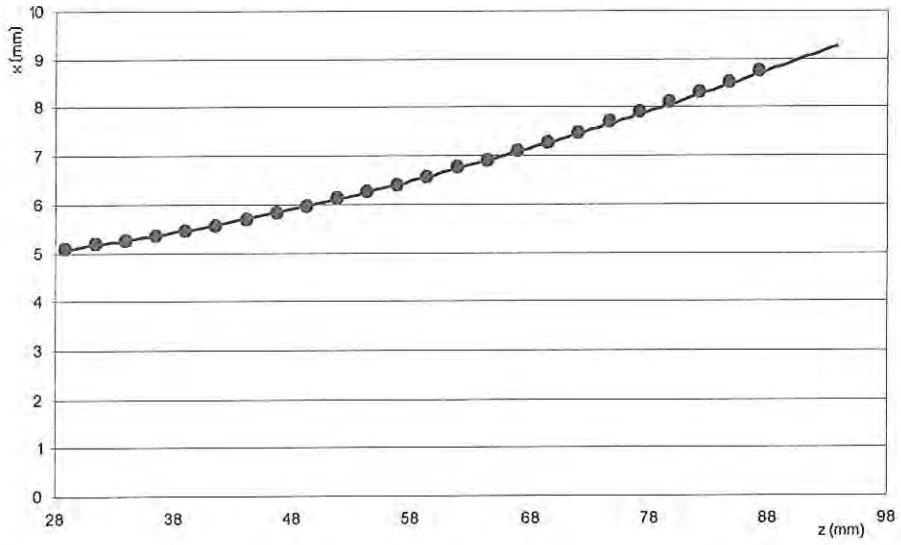

Figure 3.18 Initial beam envelope starting from aperture plate. Point is from experimental measurement and curve is from SPOT simulation

Chapter 4

Beam Matching and Calculation of Energy Spread Evolution

4.1 Characterizing the Matching Short Solenoid and Long Solenoid

Downstream of the electron gun there are three short solenoids to match the beam into the long solenoid. The energy analyzer is placed between the second and third solenoids. After the three matching lenses, there is a long solenoid, which offers uniform focusing to the beam. After the long solenoid, another short solenoid is used to make the beam match to the analysis chamber, which contains the second energy analyzer. These solenoids each have the same inner diameters of 7.6 cm. To get a solenoid with a little longer effective length, I made the third short solenoid. The current in each solenoid can be adjusted individually by different DC power supplies. A total of 5 DC power supplies is needed.

All the short solenoids were re-characterized. The fields were measured by a Bell gaussmeter with a longitudinal Hall probe. Figure 4.1 shows the measured axial magnetic field profile along the z-axis and calibration line of Peak Field B_0 versus current I inside the solenoid. The circles represent measurement points. The fitting curve is also shown in the figure. The fitted formula of the field profile for four short solenoids, M1, M2, M3 and M5 are characterized by [16]

$$B_{z0}(z) = B_0 \exp(-\frac{(z-z_0)^2}{d^2}) * \left[\sec h(\frac{z-z_0}{b}) + c \sinh^2(\frac{z-z_0}{b}) \right] \quad (4.1)$$

Here, B_0 is the maximum axial magnetic field; z_0 is the center position of the solenoids; and b, c and d are parameters to control the field profile. These parameters are different for each solenoid. Table 4.1 shows the parameters of the four short solenoids.

	M1	M2	M3	M4
b	3.4433	3.9366	5.689	5.5695
c	0.032197	0.08451	0.04654	0.061889
d	4.415	3.8872	7.2778	6.9039

Table 4.1 The parameters of the four short solenoids

The long solenoid M4 is 138.7 cm long [4]. It is made of copper windings on an aluminum tube with a diameter of 11.5 cm. There is an iron tube on the outside of the copper windings to restrict the field lines. The axial magnetic field is uniform inside the solenoid. However, at the edges, the fields decay with distance. Figure 4.1 also shows the measured axial magnetic field profile along the z-axis and calibration line of Peak B_0 versus current I. B_0 corresponds to the uniform field inside the solenoid. It depends on the beam current and the solenoid winding. The horizontal axis is the distance along the solenoid and the zero position is the physical edge of the solenoid. The fitted formula for the field profile is [4,17]

$$B_z(z) = B_0 c\left(\frac{z}{(z^2+a^2)^{1/2}} - \frac{z-l}{((z-l)^2+a^2)^2}\right) \qquad (4.2)$$

Here, c, a, and l are empirical parameters for best fitting. Their numbers are c=0.5027, a=5.0408 cm, and l=137.08 cm respectively for this long solenoid.

Mathematically, the effective length l of these solenoids can be defined by (see Page 100 in Reference [1])

$$l = \frac{1}{B_0^2} \int_{-\infty}^{\infty} B_z^2(z) dz \qquad (4.3)$$

Table 4.2 shows the effective lengths of the four short solenoids and the long solenoid.

Effective Length (cm)	M1	M2	M3	M4	M5
	4.34	4.24	7.28	130.8	7.08

Table 4.2 The effective lengths of solenoids

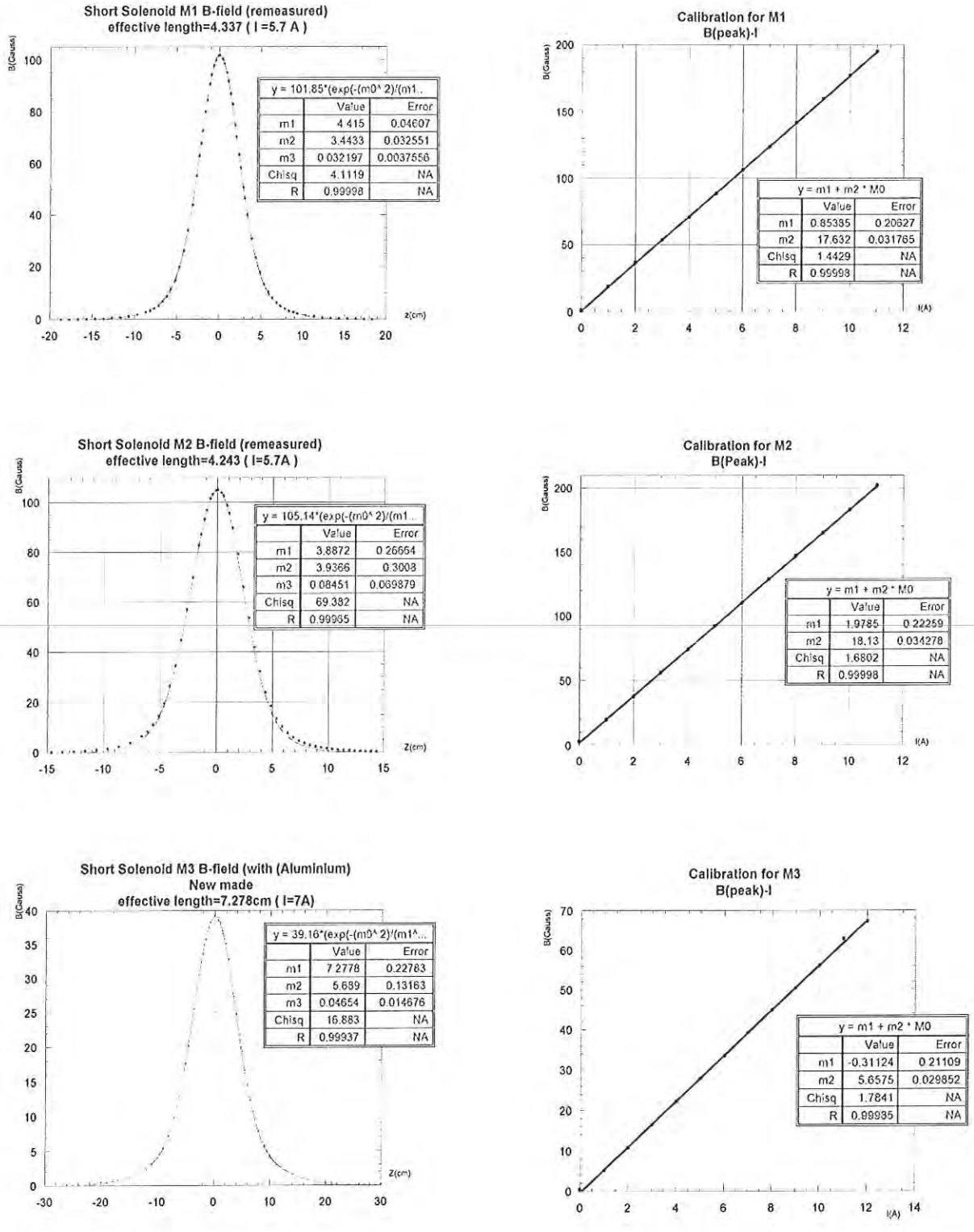

Figure 4.1 Measured axial magnetic field profile along the axis for M1, M2 and M3

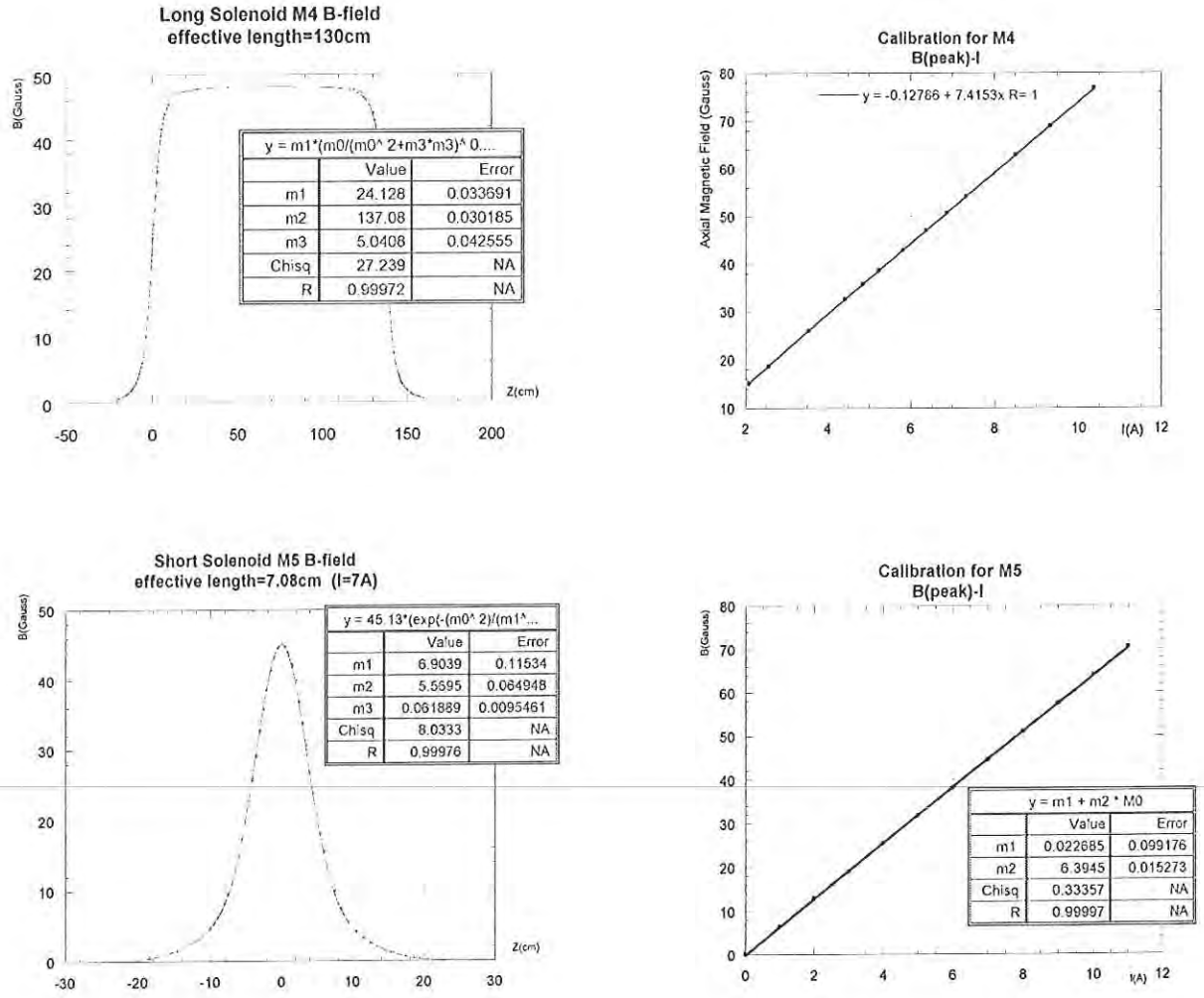

Figure 4.1 (continue) Measured axial magnetic field profile along the axis for M4 and M5

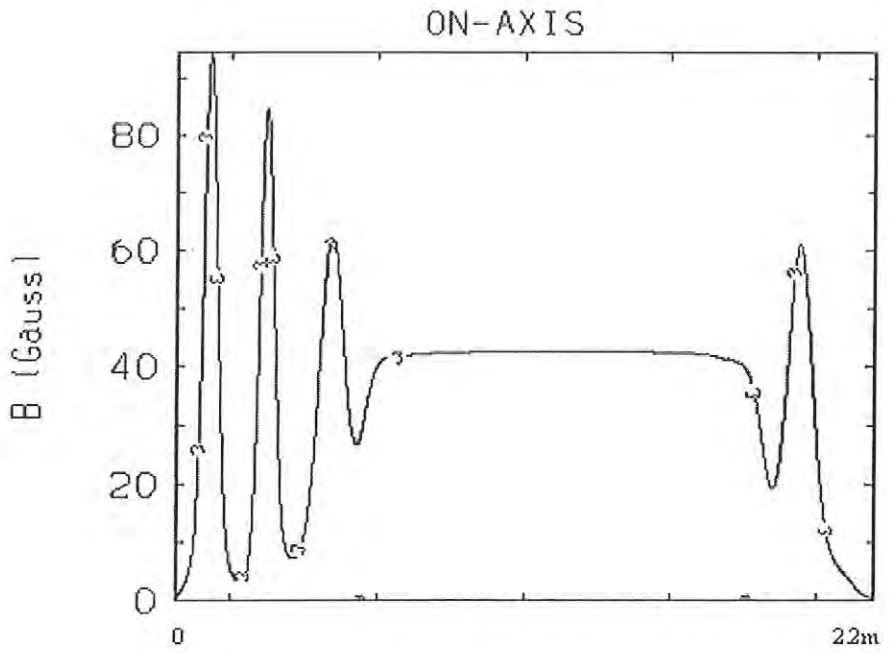

Figure 4.2 Applied Magnetic Field for 5 keV Beam

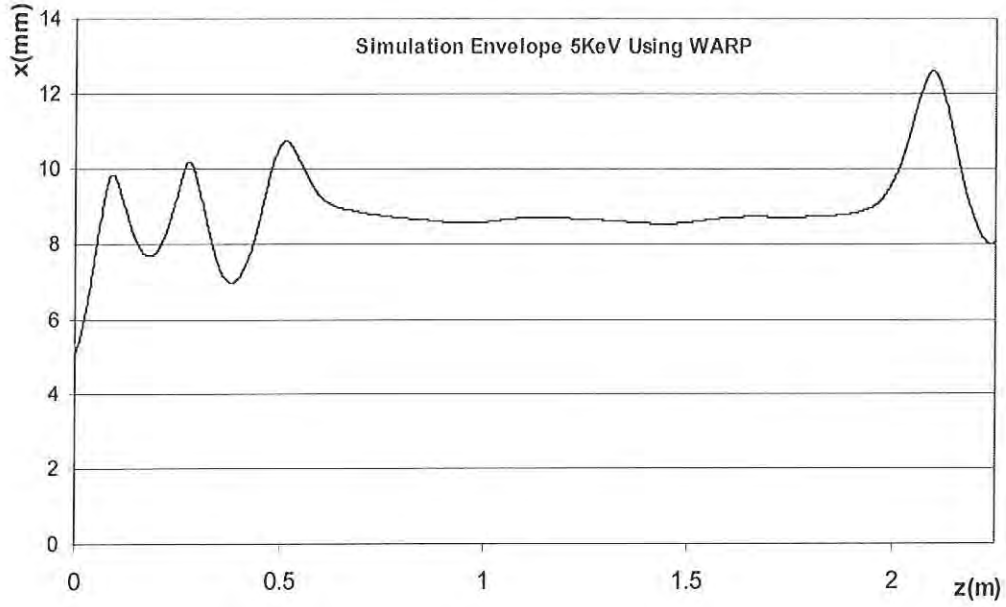

Figure 4.3 Simulation Envelope for 5 keV beam

4.2 Beam Matching

From WARP code [18] simulation, we can decide the focusing solenoid positions and focusing strength. Figure 4.2 shows the total magnetic field along z-axis needed to match the 5 keV beam. Figure 4.3 shows the matched envelope for 5 keV beams. The beam initial condition needed by the simulation comes from Chapter 3.

4.3 Calculation of Energy Spread Evolution

Let us now make a calculation of the energy spread we expect to see in our experiment. Using measurements of the beam current and simulation beam radius at a 5 kV accelerating potential, one may come up with a calculation of the relaxation time, and of the increased energy spread due to the longitudinal-longitudinal effects and the Boersch effect. Then we used Equations (2.2) and (2.4) to estimate the energy spread at various points along the z-axis.

It is easy to calculate the longitudinal-longitudinal effect because it only depends on the particle density n (see Equation 6.159 in Reference [1]) and beam energy V_0.

$$n = \frac{I}{ea^2\pi v}, \qquad (4.4)$$

where a is the beam radius which is changing along the z-axis, I is the beam current, and v is the beam velocity.

The transverse-longitudinal temperature relaxation effect is very complicated in a real beam. For an energy spread evolution experiment in which the beam propagates through a transport channel and has a varying radius, the temperature relaxation can be described by the following equation (4.5) (see Equation 6.149 in Reference [1]):

$$\frac{dT_{\perp}}{dt} = -\frac{1}{2}\frac{dT_{\parallel}}{dt} = -\frac{T_{\perp} - T_{\parallel}}{\tau} \quad . \qquad (4.5)$$

Here, $T_{\parallel}$ and $T_{\perp}$ are longitudinal and transverse temperature respectively and $T_{\parallel}$ changes twice as fast as $T_{\perp}$. Relaxation time τ is given by equation (4.6) (see Equation 6.157 in Reference [1]):

$$\tau = 4.44 \times 10^{20} \frac{(k_B T_{eff} / mc^2)^{3/2}}{n \ln \Lambda} \quad , \qquad (4.6)$$

where ln Λ is the Coulomb logarithm defined in Equation (4.7) (see Equation 6.158 in Reference [1]):

$$\ln \Lambda = \ln\left[5.66 \times 10^{21} \frac{(k_B T / mc^2)^{3/2}}{n^{1/2}} \right]. \qquad (4.7)$$

Here, $k_B T = \frac{2}{3} k_B T_{\perp 0}$, $T_{\perp 0}$ is transverse initial temperature, which is related to the cathode temperature, 0.1 eV.

Effective temperature T_{eff} is obtained from integral (4.8) (see Equation (6.151) in Reference [1]). This integral is very easy to calculate with Matlab.

$$\frac{1}{T_{eff}^{3/2}} = \frac{15}{4}\int_{-1}^{1} \frac{u^2(1-u^2)du}{\left[(1-u^2)T_{\perp} + u^2 T_{//}\right]^{3/2}} \qquad (4.8)$$

From Equation (4.7) and (4.8), we can get the relaxation time τ.

Then, From time t_{i-1} to t_i , in the time span Δt, we have:

$$T_{\perp}[i] = T_{\perp}[i-1] - \frac{T_{\perp}[i-1] - T_{\parallel}[i-1]}{\tau}\Delta t \qquad (4.9a)$$

$$T_{//}[i] = T_{//}[i-1] + 2\frac{T_{\perp}[i-1] - T_{\parallel}[i-1]}{\tau}\Delta t \qquad (4.9b)$$

Here, $\Delta t=(z_i-z_{i-1})/(\beta c)$, z_i is distance from the anode along the z-axis and initial temperature $T_{//}[0]$ is 0 and $T_{\perp}[0]$ is equal to $T_{\perp 0}$.

Matlab was used to do this numerical calculation (see Appendix 1), and the calculation result is shown in Figure 4.4. The energy spread at the beam waist, roughly 37 cm from the anode, is 1.4 eV, and at 2.2 m from the anode is 3.8 eV.

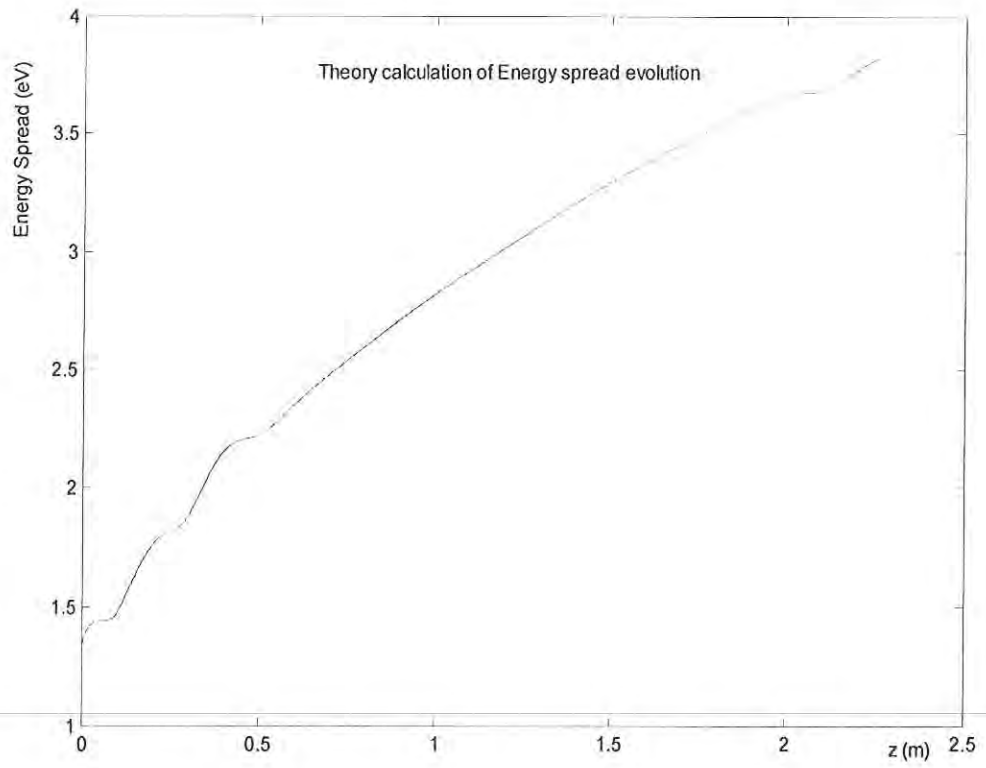

Figure 4.4 Theoretical Calculation for Energy Spread Evolution of 5 keV

Chapter 5

Design of New High-Performance Energy Analyzer

5.1 Introduction

According to the calculation in the last chapter, the energy spread over a distance of 0.37 m is 1.4 eV, and 3.8 eV over 2.25 m for a 5 keV beam. To measure such small energy spreads the energy analyzers must have good resolution. Also, University of Maryland Electron Ring (UMER)[7], currently being constructed, requires detailed knowledge of the beam's energy spread. The energy spread of the beams from the thermionic gun and the evolution of this energy spread in the beam transport line must be measured with good accuracy. So a high-resolution energy analyzer is highly needed. Retarding field energy analyzers have high signal-to-noise ratio outputs and their structure is simple so they have been widely used to measure the energy spread of low energy beams.

5.2 Theory of Retarding Field Energy Analyzer

The simplest retarding field energy analyzer is the parallel plate energy analyzer as shown in Figure 5.1a [4]. If the beam is ideal, all the electron trajectories are parallel to the beam axis. The beam enters the energy analyzer through a hole, and is retarded by the retarding voltage. The kinetic energy of the electrons is converted into potential energy. The electrons whose kinetic energy is higher than the retarding potential can pass this retarding potential and reach the

collector to form the current. Other electrons will be reflected. Hence, if the beam is mono-energetic, the ideal response of the energy analyzer should have a sharp cut-off at the beam energy, as shown in the Figure 5.1(b) [4]. In reality, for our case, when electrons are emitted from the electron gun, the beam has a finite divergence angle because of emittance, space-charge effects and misalignment. The axial kinetic energy overcoming the retarding potential is related to the total beam energy by [4]

$$E_{\parallel} = E_t (\cos\theta)^2 . \qquad (5.1)$$

That means even though all the electrons have the same total kinetic energy, there always exists an inherent energy spread which is expressed by (5.2) in this parallel plate energy analyzer [4]

$$\Delta E = E_t - E_{\parallel} = E_t \sin^2\theta \qquad (5.2)$$

The larger this divergence angle, the worse the energy spread measurement resolution will get. So we would like to find a way to try to restrain the transverse motion of the electrons to reduce this inherent energy spread of the energy analyzer.

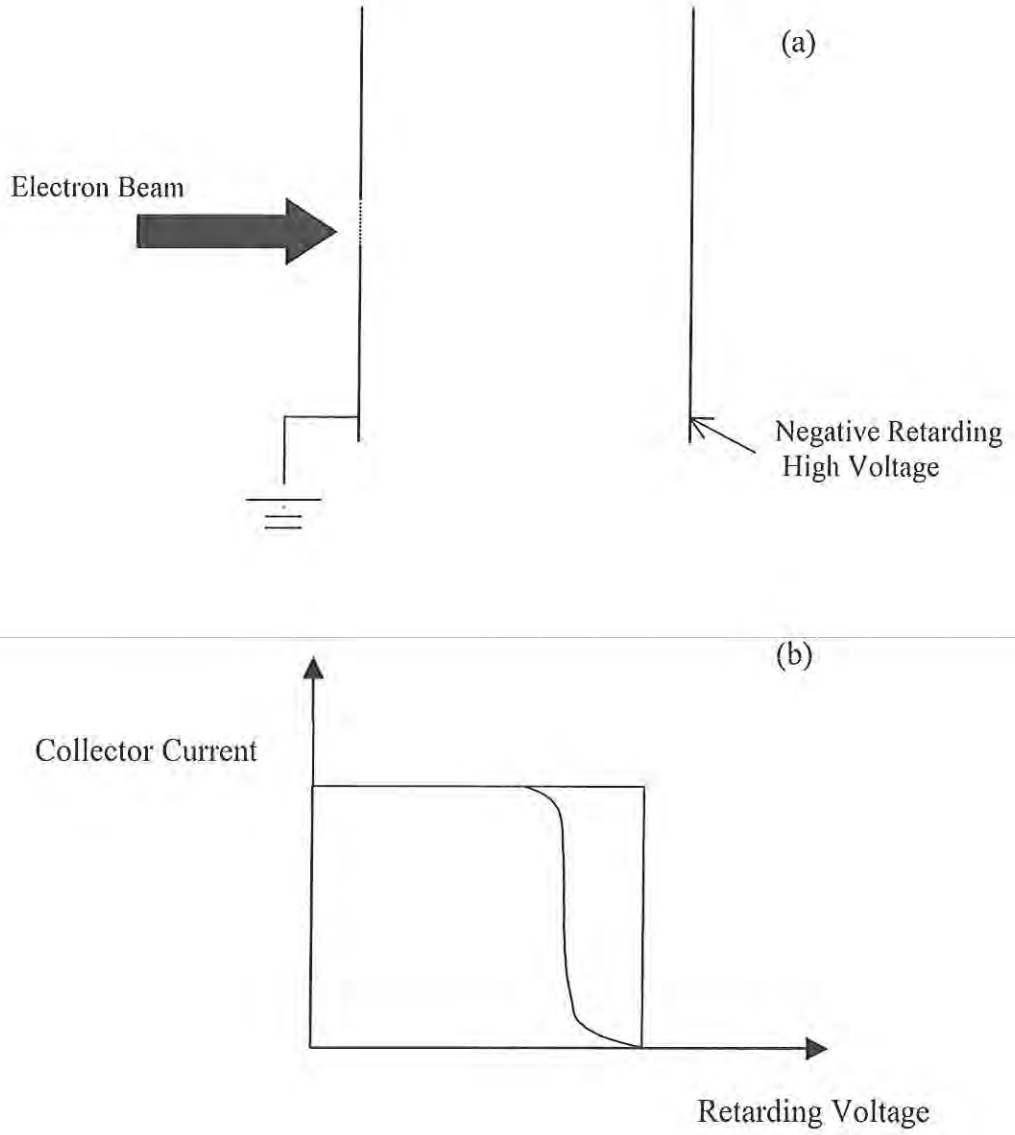

Figure 5. 1 (a) Theoretical schematics of Retarding Field Energy analyzer.

(b) Responses of ideal and real energy analyzers to a monoenergetic beam.

5.3 Cylindrical Retarding Energy Analyzer and Improved Design

Energy spread measurements were made in the UMER lab using a Parallel plate energy analyzer. For a 5 keV beam, test results show the energy spread is more than 20 eV [19,20], which is much larger than the theoretical calculated value.

A previous PhD student, YunZou, designed a cylindrical retarding field energy analyzer (Figure 5.2) that has a smaller inherent energy spread than a parallel electrode analyzer [4]. The focusing cylinder inner diameter is ϕ26 mm and its length is 25 mm. The end of this cylinder is covered with mesh to keep the retarding voltage out of the cylinder. When the electron axial kinetic energy is bigger than the retarding voltage, it crosses the mesh, is collected by the collector, and forms a current signal. The grounded housing has a hole with a diameter of 1 mm and it is covered with wire mesh to produce a uniform electric field preventing defocusing. The test result shows it greatly improved the resolution compared to the parallel-plate energy analyzer used before. The idea of this design is to use curved equipotential lines to give transverse electric focusing to the beam in the cylinder shown in Figure 5.2. For a 5 keV beam, the resolution can get to 2 eV.

UMER uses this cylindrical geometry energy analyzer design. In order to get a stronger collector signal, the hole in the grounded housing is increased from 1 mm to 2 mm in diameter.For a 10 keV beam, the test result shows the energy spread is about 8.5 eV [21], which is much larger than that predicted by theoretical

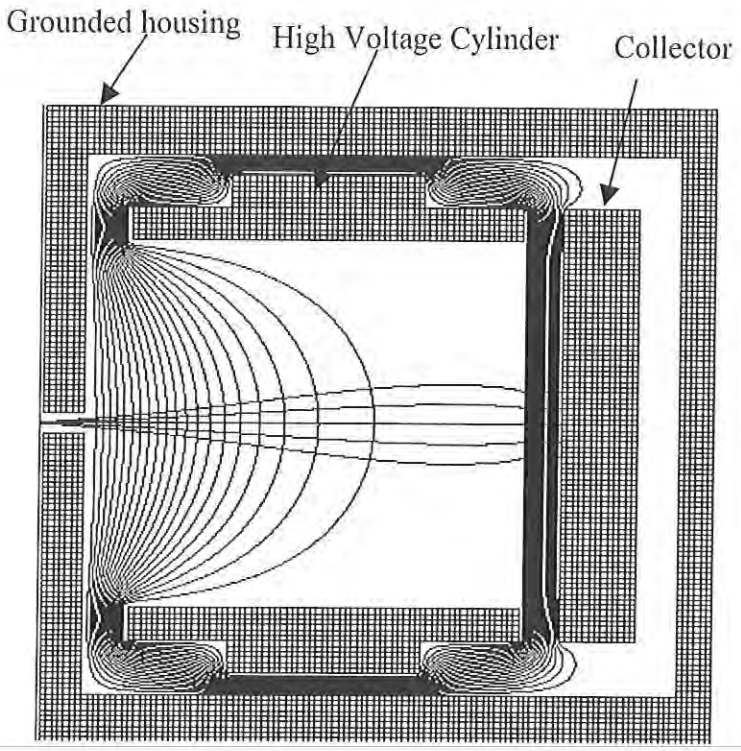

Figure 5. 2 Schematics of cylindrical energy analyzer with equi-potential lines and typical particle trajectories.

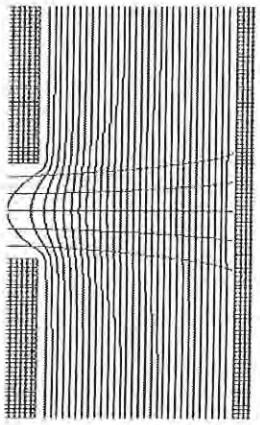

Figure 5. 3 Defocusing effect of an aperture in the plate

calculations. SIMION [22] simulation results show the resolution of this kind energy analyzer is 8 eV for a 10 keV beam. The real beam energy spread may be shadowed by the inherent resolution of the energy analyzer.

After analysis, we found that the poor resolution is related the focusing field. If the hole is too big, it is very difficult to focus all the electrons onto the collector. Also, the aperture effect of the hole without mesh will cause beam defocusing near the hole as shown in Figure 5.3. So we need to use a wire mesh covering on the aperture.

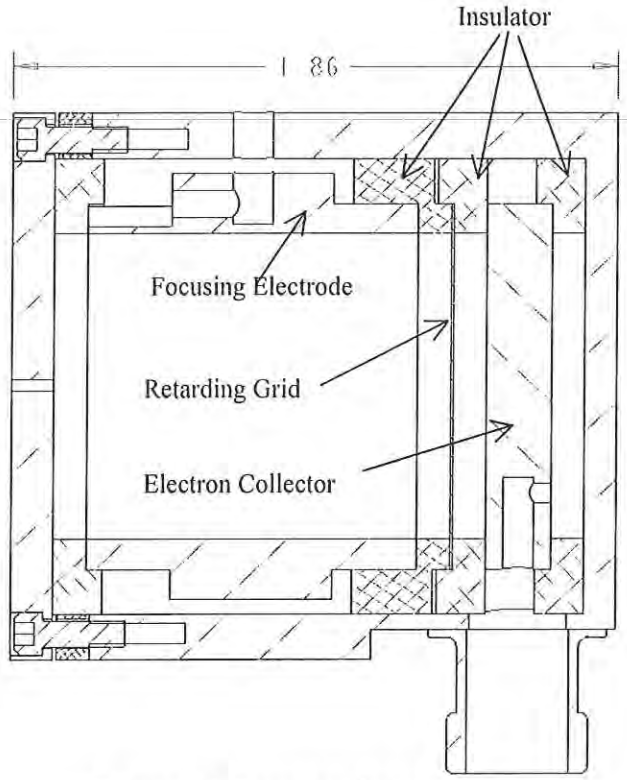

Figure 5.4 Cross-sectional view
of new designed energy analyzer

Since the goal of such a design is to focus incoming electrons onto the collector in such a manner that they come as close as possible to impinging perpendicularly upon the retarding grid, we can try to apply a little higher focusing voltage on it to increase electron collection by the collector.

In the previous energy analyzer the focusing electrode and the retarding grid were electrically connected. We have altered this design somewhat so that we may have the focusing electrode at a separate potential from the retarding grid. Figure 5.4 shows a cross-sectional view of the newly designed analyzer [23]. The diameter of the hole is 2 mm. The focusing electrode is a cylinder separated with wire mesh using good insulating material. A cable is connected to the collector to get the output signal. Simulations of this design using SIMION were completed and compared with the previous design, indicating that the resolution of the energy analyzer may be improved significantly, from 8 eV to 0.5 eV for a 10 keV beam. For the previous design, Figure 5.5 shows the electron trajectories from SIMION simulation and Figure 5.6 is the corresponding simulated performance when a 10 keV beam with a 0.5° angular spread enters the energy analyzer. For the new design, Figure 5.7 shows the electron trajectories and Figure 5.8 is the corresponding simulated performance when the focusing voltage is 130 V higher than the retarding voltage and the beam is the same as the previous one.

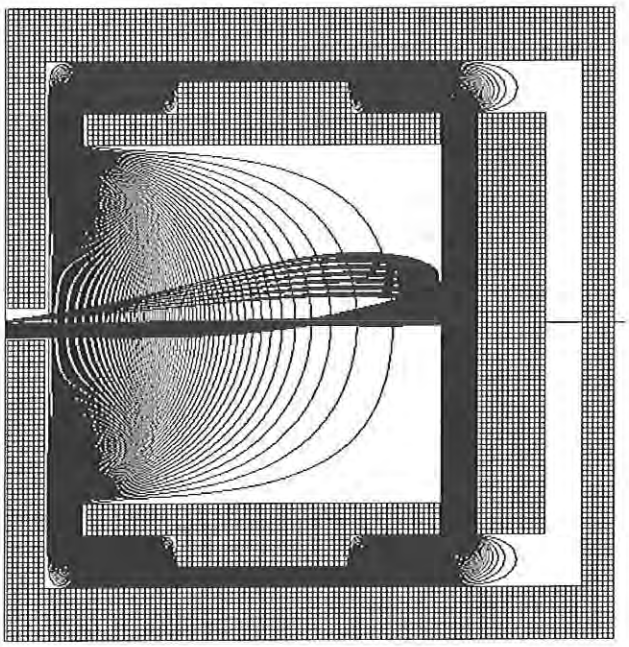

Figure 5.5 Focusing cylinder connected to the Grid, retarding voltage is -9999.5 V, beam is 10 keV

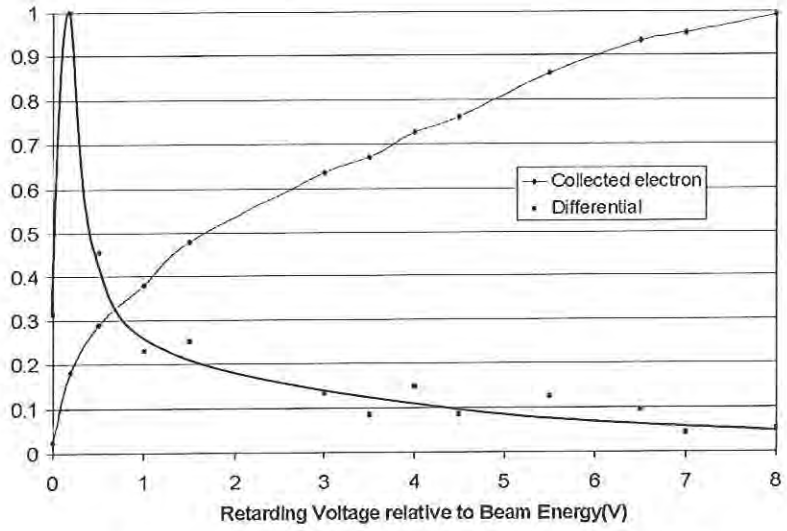

Figure 5.6 Previous Energy Analyzer Resolution (10 keV Beam, By Applying same Focusing Voltage)

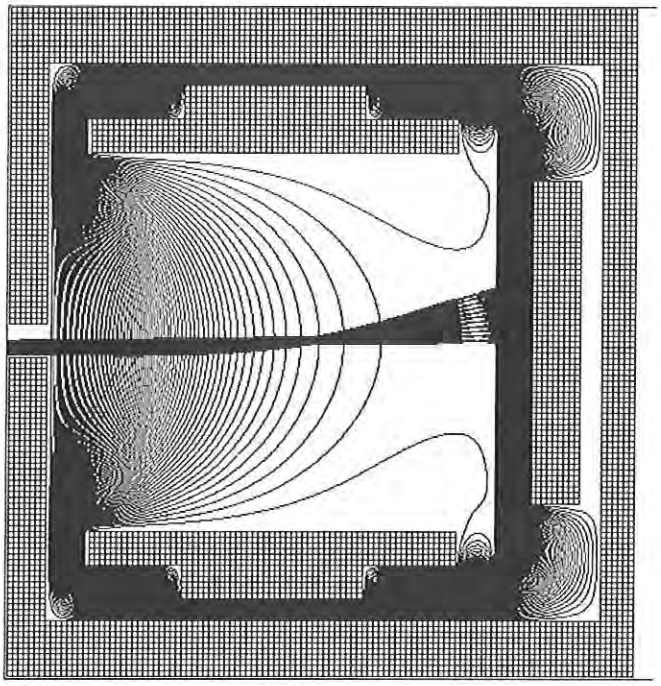

Figure 5.7 Focusing cylinder separated with Grid, retarding voltage is -9999.5 V, focusing voltage is –10130 V, beam is 10 keV

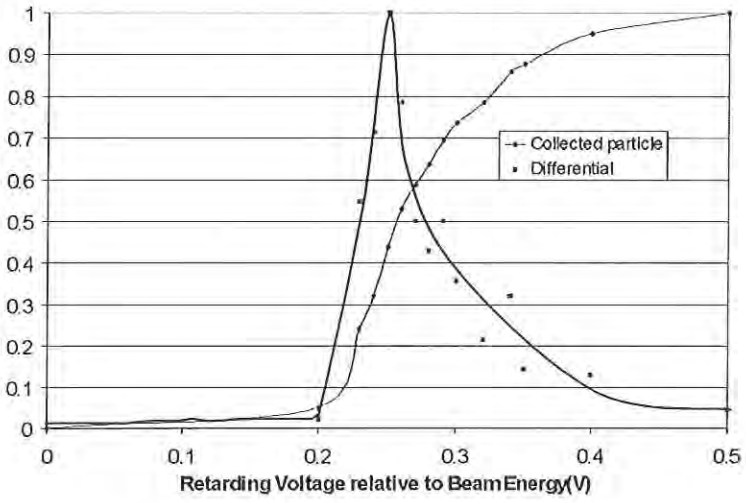

Figure 5.8 Energy Analyzer Resolution Improvement Result (10 keV Beam, By Applying 10.13 kV Focusing Voltage)

For different beam energies, the energy analyzer resolutions are different. The higher the beam energy, the less resolution the energy analyzer has. Table 5.1 shows the energy analyzer resolution and voltage difference between the focusing electrode and the retarding voltage at 3 keV, 5 keV and 10 keV for new design.

Beam Energy	3 keV	5 keV	10 keV
Energy Analyzer Resolution	0.15 eV	0.25 eV	0.5 eV
Voltage Difference	40 V	65 V	130 V

Table 5.1 Energy Analyzer Resolution for different energy beam

5.4 Time Response Measurement of the Energy Analyzer

There is capacitance existing between the plate collector and the grounded housing in the energy analyzer. Since we know the dimensions of the energy analyzer, it is very easy to calculate the value of this capacitance, which is found to be about 8 pF. We would like to know how strongly this capacitance effects the output signal.

The energy analyzer's equivalent circuit is shown in Figure 5.9 [24]. A current signal is input into an RC circuit. The R is the 50 Ω characteristic impedence of the transmission line.

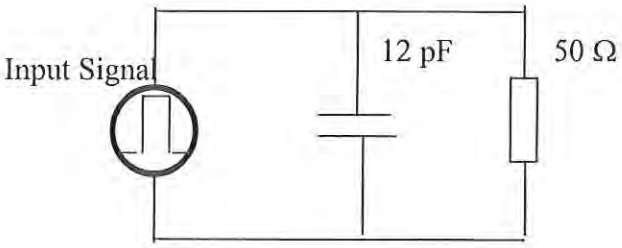

Figure 5.9 Equivalent Circuit of Energy Analyzer

Two current input signals were used to test the output time response of the energy analyzer. The experimental result in Figure 5.10 shows that an input signal with a 4 ns rise time generates an output signal with a 10 ns rise time and an input signal with 1.5 ns rise time generates an output signal with a 4 ns rise time. The output waveform is good and indicates no major noise inside the energy analyzer. Comparing with the equivalent circuit simulation result from PSPICE [25], we find the total capacitance, composed of equivalence capacitance and systematic distributed capacitance, of the energy analyzer is about 12 pF. Frequency bandwidth is about 1.6 GHz. This is a much larger bandwidth and collector cause very little distortion to the signal, so the output signal of the energy analyzer is acceptable.

Experimental Result

Pspice Simulation Result

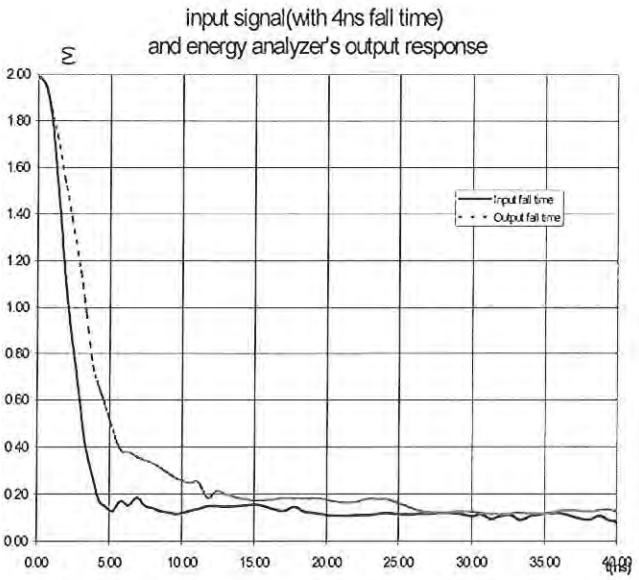

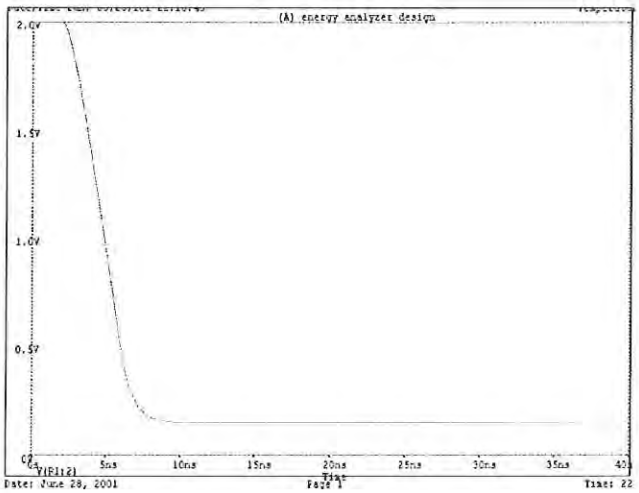

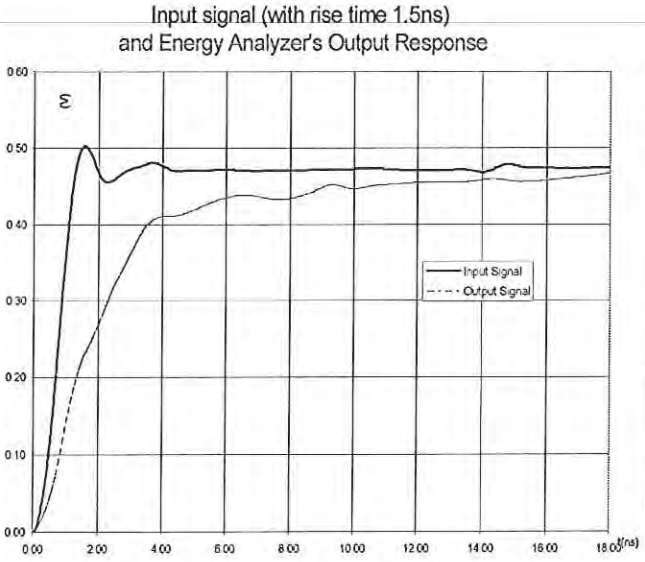

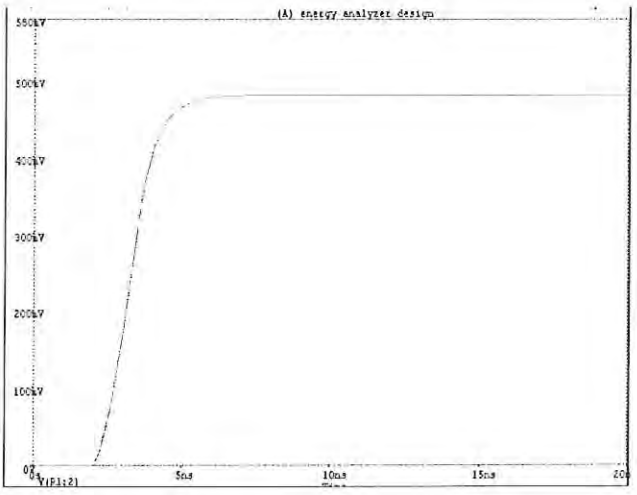

Figure 5.10 Time Response Experimental Result in Comparison with the PSPICE Simulation Result

Chapter 6

Conclusion

I have performed a series of experiments to calibrate the electron gun: characterize its performances and obtain the initial beam conditions. This experiment is the preparation for the energy spread evolution experiment. The UMER gun has the same structure as this gun. The only differences are some modifications in gun control electronic circuit. The performance characteristics of this gun will be compared with that of UMER gun.

The pulser signal of the electron gun had a very strange tail that caused the poor shape of the beam pulse. By studying the generation of pulser signal, a theoretical explanation was given for the pulser signal tail and the mismatched impedance was found between the pulse forming line and the emitter of the transistor. After a 75 Ω coaxial cable replaced the 50 Ω coaxial cable as the pulse forming line, a good pulser signal was achieved in the experiment and there was nearly no tail in the pulser signal.

Calculation results for 5 keV beam, showed that energy spread growth of the space-charge dominated beam caused by the Boersch effect and the longitudinal-longitudinal effect is 2.4 eV. Measuring such a small energy spread is challenging. An improved design of the cylindrical energy analyzer was done and its simulated resolution is 0.5 eV for 10 keV beam. This energy analyzer is

currently being built and will soon be tested to determine whether performs as deigned and can be therefore used to characterize the energy profile of electron beam with high resolution.

A transport line with the length of 2.2 m is being set up to study the energy spread evolution. The newly designed energy analyzer will be a promising tool to study the beam energy profile at the two points along the transport line. We are able to measure the energy spread evolution due to the Boersch effect and the longitudinal-longitudinal relaxation effect.

After the energy spread evolution experiment, we will be in a position to use perturbation on the beam to study the resistive-wall instability.

Appendix 1

Matlab program to calculate energy spread

```
% This program is to calculate energy spread along the distance,
% It consider the boserch effect and longitudinal effect.
syms u real;
ek=5;       % beam energy
current=0.135;     %beam current
c=3*10^8;       % light speed
rc=0.004;     %cathode radius(mm)
kbtc=0.1;     %cathode temperature 0.1eV
fid = fopen('c:\thesis\5kevout1_non.dat','W');
gama=(ek+511)/511;
beta=sqrt(1-1/gama^2);

fin = fopen('c:\thesis\5kev.txt','r');
[temp,count]=fscanf(fin,'%g');
for i=1:count/2
   L(i)=temp(2*i-1);
   a(i)=temp(2*i)*0.001; % change to unit-m from unit-mm
   n1=current/(1.6*10^(-19)*a(i)^2*pi*beta*c);
   if i==1
      kbttra(1)=kbtc*(rc/a(i))^2;
      kbtpara(1)=0;

   else
      logramd=log(5.66*10^21*(2/3*kbttra(1)/511000)^1.5/n1^0.5);
      temp1=15/4*int(u^2*(1-u^2)/((1-u^2)*kbttra(i-1)
               +u^2*kbtpara(i-1))^1.5,-1,1);    % do integrate
      kbTeff=(1/temp1)^(2/3);
      kbTeff=double(kbTeff);
      tao=4.44*10^20*(kbTeff/511000)^1.5/(n1*logramd);
      t=L(i)/beta/c;
      deltaL=L(i)-L(i-1);
      kbttra(i)=kbttra(i-1)-(kbttra(i-1)-kbtpara(i-
1))/tao*deltaL/(beta*c);
      kbtpara(i)=kbtpara(i-1)+2*(kbttra(i-1)-kbtpara(i-
1))/tao*deltaL/(beta*c);

      % kbtpara(i)=kbtpara(i-1)+2*kbttra(1)*exp(-
3*t/taoeff)*deltaL/(beta*c*taoeff);

   end
   delte1(i)=(2*ek*1000*kbtpara(i))^0.5;
   n2=current/(1.6*10^(-19)*a(i)^2*pi*beta*c);
   second(i)=(4.8*10^(-10))^2*(n2/10^6)^(1/3)/(1.6*10^(-12));
   delte2(i)=(kbtc^2+second(i)*4*ek*1000)^0.5;
   deltE(i)=(delte1(i)^2+delte2(i)^2)^0.5;
```

```
    fprintf(fid,'%8.4f,%8.4f \n',L(i),deltE(i));
    i=i+1;
end
fclose(fin);
fclose(fid);

figure(1);
plot(L',delte1);
figure(2);
plot(L',delte2);
figure(3);
plot(L',deltE);
clear;
```

References

[1] M. Reiser, Theory and Design of Charged Particle Beams (John Wiley & Sons, Inc, New York,1994).

[2] V. V. Aleksandrov, N. S. Dikansky, N. C. Kot, *et al.*, Phys. Rev. A, **46**(10) 6628 (1992).

[3] H.Boersch, Z.Phys. 139,115 (1954)

[4] Yun Zou, Ph.D. Dissertation, Department of Electrical Engineering, University of Maryland, 2000

[5] S. Ichimaru and M. N. Rosenbluth, Phys. Fluids 13, 2778 (1970)

[6] J.G. Wang, E. Boggasch, et al., Performance Characteristics of a Variable-Perveance Gridded Electron Gun, IEEE transactions on electron devices, Vol. 37. No. 12. Dec. 1990

[7] P.G. O'Shea, M. Reiser, et al., The University Maryland Electron Ring (UMER), Nuclear Instruments and Methods in Physics Research A 464 (2001) 646-652

[8] S. Bernal, Ph.D. Dissertation, Electrical Engineering Department, University of Maryland at College Park, 1999.

[9] Paul R.Gray /Robert G. Meyer, Analysis and Design of Analog Integrated Circuits, John Wiley& Sons, Inc., 1993

[10] Omp. Gandhi, Microwave Engineering and Applications, Pergamon Press, 1981.

[11] J.C. Slater, Microwave Electronics, D. Van Nostrand Company, 1950

[12] Zhiyuan Shen, Microwave theory (Chinese), Defense Industry press, 1980

[13] Maozhang Gu, Perturbation in the measurement of microwave field, Applied Science newspaper(Chinese),vol.4(2), 1986

[14] Frank J. Sacherer, et al., RMS Envelope equations with space charge, IEEE tran. Nucl. Sci 18, 1971

[15] SPOT Document

[16] R. Kishek, New empirical formula for IPR solenoids, code: E-RING-97-53

[17]. John David Jackson, Classical Electrodynamics, John Wiley& Sons, Inc., 1998

[18] WARP Document

[19] H. Suk, Ph.D. Dissertation, Physics Department, University of Maryland at College Park, 1996.

[20] N. Brown, Ph.D. Dissertation, Physics Department, University of Maryland at College Park, 1995

[21] A. Valfells, Y. Cui, et al. PAC Conference, 2001, Chicago

[22] SIMION Document

[23] Y. Cui, A. Valfells, et al. PAC Conference, 2001, Chicago

[24] Curtis L. Hemenway, et al. Physical electronics, John Wiley and Sons, Inc. 1967

[25] PSPICE Document